ABSTRACT

Title of Document: AUTOMATED QUANTIFICATION AND CLASSIFICATION OF HUMAN KIDNEY MICROSTRUCTURES OBTAINED BY OPTICAL COHERENCE TOMOGRAPHY

Qian Li, Master of Science, 2009

Directed By: Assistant Professor, Yu Chen, Department of Bioengineering

Optical coherence tomography (OCT) is a rapidly emerging imaging modality that can non-invasively provide cross-sectional, high-resolution images of tissue morphology such as kidney *in situ* and in real-time. Because the viability of a donor kidney is closely correlated with its tubular morphology, and a large amount of image datasets are expected when using OCT to scan the entire kidney, it is necessary to develop automated image analysis methods to quantify the spatially-resolved morphometric parameters such as tubular diameter, and to classify various microstructures. In this study, we imaged the human kidney *in vitro*, quantified the diameters of hollow structures such as blood vessels and uriniferous tubules, and classified those structures automatically. The quantification accuracy was validated. This work can enable studies to determine the clinical utility of OCT for kidney imaging, as well as studies to evaluate kidney morphology as a biomarker for assessing kidney's viability prior to transplantation.

AUTOMATED QUANTIFICATION AND CLASSIFICATION OF HUMAN KIDNEY MICROSTRUCTURES OBTAINED BY OPTICAL COHERENCE TOMOGRAPHY

By

Qian Li

Thesis submitted to the Faculty of the Graduate School of the

University of Maryland, College Park, in partial fulfillment

of the requirements for the degree of

Master of Science

2009

Advisory Committee:
Assistant Professor Yu Chen, Chair
Associated Professor Keith Herold
Assistant Professor Frank Siewerdt

Acknowledgements

I would like to thank my advisor Dr. Yu Chen for having given me this opportunity to work on this project and for all the time, help and encouragement that he has given me over the course of its development.

I would like also to thank my lab mate Chao-wei Chen who has helped on the pre-analysis of the data classification, Dr Peter Andrews and Maristela, who supplied the preparation of the experiment objects and gave me plenty of explanations of the data results.

I would like also to thank my colleagues at the university – Dr. Shuai Yuan, Renee, Jerry, Anik, Bobak, Dennis, and Dipankar for everything from technical discussions, insight and suggestions.

On a personal note I would like to thank my family, who gave me endless support all the time.

This work is supported in part by the Nano-Biotechnology Award of the State of Maryland, the Minta Martin Foundation, the General Research Board (GRB) Award of the University of Maryland, the University of Maryland Baltimore (UMB) and College Park (UMCP) Seed Grant Program, the Prevent Cancer Foundation, and the National Kidney Foundation of the National Capital Area.

Table of Contents

List of Figures

List of Acronyms and Abbreviations

3D	Three Dimensional
A – scan	Line depth scan
B – scan	Vertical plane scan
CT	Computed Tomography
FOV	Field of View
FWHM	Full Width at Half Maximum
HIST	Histogram
MRI	Magnetic Resonance Imaging
OCT	Optical Coherence Tomography
ROI	Region of Interest
STD	Standard Deviation

CHAPTER 1

1 INTRODUCTION AND MOTIVATION

Optical coherence tomography (OCT) is a rapidly emerging imaging modality that allows high resolution, noninvasive, cross-sectional imaging of tissue morphology *in situ* and in real-time [1]. OCT is analogous to ultrasound, however, OCT generates images by measuring the back reflection intensity of light instead of sound wave. Although the light scattering properties of biological tissues typically limit light penetration to less than 2 mm, this imaging depth has proven sufficient to provide valuable information about tissue pathology in a number of biomedical fields. Therefore, OCT is a promising imaging modality to assess tissue pathologies *in situ* and in real time. In addition, image processing has evolved to play an important role in understanding the information content of biological tissues [2-5].

1.1 Current trends in OCT technique

In the recent decades, OCT has been widely used in diagnosis and computer-guided surgery. Numerous literatures have been reported applying OCT in different biomedical fields, including ophthalmology [6-8], cardiology [9, 10], and gastroenterology [11-14]. In certain areas, such as ophthalmology, proven products have been developed from OCT to serve as prime tools in clinical offices. Furthermore, OCT can be interfaced with various imaging devices such as catheters, endoscopes, laparoscopes, and needles, with typical image resolutions of 1-15 μm [15], to provide broader applications in biomedical area.

1.2 Significance of kidney images obtained by OCT

A kidney transplant is often the most ideal treatment option for kidney failure [16], and according to the National Kidney Foundation there are approximately seventy thousand patients awaiting kidney transplants per year in the U.S. One severe problem for kidney transplant is post transplant renal failure due to kidney deterioration during the storage. Therefore, a reliable and accurate test is needed to evaluate the viability of donor kidney and predict post-transplantation renal function.

The viability of a donor kidney is closely correlated with its tubular morphology [17]. OCT enables three-dimensional visualization of the kidney microstructures, thus can assist in the evaluation of donor kidneys. Compared with conventional microscopy, Computed Tomography (CT), Magnetic Resonance Imaging (MRI) and ultrasound, the versatility of OCT imaging procedures, its resolution capabilities and increased depth analysis make OCT an ideal method for imaging the human kidney *in situ* and in real time.

Prior studies utilized non-human kidneys for OCT imaging analysis, while this study uses OCT to study the human kidney ex vivo. Various structures from different human kidneys were readily distinguished, including the blood vessels, uriniferous tubules, glomeruli, and kidney capsules. The methods of this study could be directly applied to donor kidney viability analysis, since the previous study [17] indicated that proximal tubular structure and post-transplantation renal function are closely correlated. In addition, there are existing correlations between glomerular morphology and renal diseases, i.e. mesangial proliferative glomerulonephritis [18], focal segmental glomerulosclerosis [19], Type I diabetes mellitus [20], and renal ischemia [21].

Therefore, OCT's ability to distinguish glomeruli structures is a potentially valuable tool for the diagnosis of glomerular diseases as well.

OCT imaging can provide immediate information regarding the histopathological status of the renal vasculature, tubules, and glomeruli. One potential OCT application is the evaluation of the viability of donor kidneys [22]. Previous studies using tandem-scanning confocal microscopy [17] indicated that proximal tubular structure and post-transplantation renal function are closely correlated. In a recent study [23], living rat kidneys were observed *in vivo* before, during, and after an ischemic insult using OCT, which enabled the visualization and comparison of the rat kidney morphology. OCT therefore represents an exciting new approach to visualize, in real-time, the pathological changes in the living kidney in a non-invasive or minimally invasive fashion.

1.3 Motivation for developing automated algorithms

In an earlier study [23], the total volume of the kidney tubules were segmented and quantified. Statistically significant changes were observed during the ischemia. However, the segmentation algorithm used in this prior study quantified the average tubular volume changes only, and the spatially-resolved local morphological changes were not able to be separated and quantified. Furthermore, kidney structures are heterogeneous; therefore the difference in tubular volume is confounded by the tubular density. Another earlier study [17] suggested that the tubular lumen diameter is a more robust biomarker for kidney viability, and a decrease in lumen diameter during ischemia was observed visually by both confocal microscopy [17] and OCT [23]. Therefore, it is important to develop methods to quantify the spatially-resolved tubular diameters.

The most straight-forward method to quantify the tubular diameters from OCT (or other imaging modalities) images is manual measurement using calipers or partially-automated image analysis software, i.e. ImageJ. Although accurate and reproducible measurements can be obtained in this way, an obvious drawback is the extent of user interaction required for the analysis. For instance, it requires manual selection of the region-of-interest (ROI) and the tubular wall edges on the images by the operator as the first step. This procedure is very laborious and time-consuming, which precludes the possibility of analyzing large amounts of data. This is especially challenging for OCT imaging of the kidney, since individual OCT images have a field-of-view (FOV) of several millimeters while a typical human kidney has a surface area larger than 10 cm by 10 cm. To provide an accurate assessment of the entire kidney, comprehensive OCT imaging is necessary, which would involve a large number of images from various locations of the kidney. Thus, an automated image analysis method is critical.

Our previous work has demonstrated that hollow kidney microstructures such as uriniferous tubules and Bowman's space can be automatically segmented based on their different backscattering intensities [23]. Automated segmentation of colonic crypt morphology using OCT [4] has also been demonstrated. In addition, automatic evaluation of diameters of a single cylindrical structure such as brachial artery has been demonstrated using B-mode ultrasonic imaging [24, 25]. However, in our application, multiple isolated tubules with various diameters and curvatures are presented in a single OCT image. To obtain the spatially-resolved morphometric information, it is necessary to separate those isolated regions for further quantification. The purpose of the present study was to develop an image processing method for automated selection of individual ROI and quantification of the size of the hollow structures in the kidney, including renal

tubules, glomeruli, and vessels. Since there are significant differences in the size and structure of human kidneys and those of rodents, we undertook these studies using human kidneys for enhanced clinical relevance. This study is a necessary step before assessing the utility of OCT in clinical evaluation of kidney viability.

In summary, a large number of image datasets are expected when using OCT to scan the entire kidney to provide a global assessment of its viability, so it is necessary to develop automated image analysis methods to quantify the spatially-resolved morphometric parameters such as tubular diameter.

1.4 Overview

The objective of this study is to realize automated quantification and classification of human kidney microstructures from images obtained by OCT to provide potential diagnostic information of donor kidney.

This thesis is based on the following topics. Chapter 2 will describe the materials and experimental setup. Chapter 3 will be an overview of the image preprocessing. Chapter 4 will demonstrate the image feature quantification and results while in Chapter 5 the methods and results of the image classification will be presented. Chapter 6 is the summary and discussion of the work and an insight into future work.

CHAPTER 2

2 EXPERIMENTAL SETUP

2.1 Human kidney and histology

This study protocol was approved by the Institutional Review Boards (IRB) at both the University of Maryland and Georgetown University. Four donor kidneys were obtained through the Washington Regional Transplant Consortium (WRTC). Upon arrival, the kidneys were fixed by vascular perfusion with 10% neutral formalin (through the renal artery) to preserve their renal morphology. After the OCT image acquisition, the location and direction of each scanned section were marked with ink, for subsequent standard histology processing. For conventional light microscopy, 4 µm thick sections were cut, stained with hematoxylin-eosin (H&E), and photographed with a Nikon Eclipse 80i (Nikon, Melville, NY) attached to a digital camera Nikon DS-Fi1 (Nikon). The micrographs were obtained for comparison with the OCT images.

Fig. 1. The photo of one of the human kidneys imaged by OCT.

2.2 Optical coherence tomography (OCT) imaging

OCT technology is based on low coherence interferometry. The interference in OCT is in the range of micrometers, thus requiring the use of broadband light sources. In OCT system, the light source is divided into two branches or arms - a sample arm which holds the object of interest and a reference arm which is typically a mirror. The combination of reflected lights from both arms (sample arm and reference arm) can result in an interference pattern if the optical distance of the light in each of the arm has traveled comparable distances. This occurs when the difference of optical distances is less than a coherence length. There will be no interference of any light outside this short coherence length. Therefore, areas of the object which reflect back light will create greater interference than areas that do not. The reflectivity profile is known as an A-scan, consisting of the location of structures within the object of interest and also information about the spatial dimensions. A cross-sectional tomographe, known as B-scan, may be achieved by combining laterally a series of these axial depth scans (A-scan). En face imaging (C-scan) at an acquired depth is possible, but depends on the imaging engine used.

This study used a high-speed high-resolution OCT system (Thorlabs Inc., NJ, USA) using swept source/Fourier domain detection that enabled three-dimensional (3D) OCT imaging *in situ*. The light source was a wavelength-swept laser light source generating a 100 nm full width at half maximum (FWHM) bandwidth at 1310 nm, yielding an axial resolution of 10 µm in the tissue. The laser operated at a swept rate of 16 kHz with an average output power of 12 mW. The imaging frame rate was 30 frames per second. The transverse resolution of the system was 15 µm with 4 mW of power illuminating the sample.

Fig. 2 shows the overall schematic of the OCT system used in this experiment. The inset in the lower left corner shows the imaging microscope. The output of the swept laser was split into two portions: three percent was used to generate a clock signal for triggering the sample of the OCT signal on a uniformly-spaced optical frequency grid [26]; the remaining ninety-seven percent of the output was equally distributed to the OCT sample and reference arms. Imaging of the human kidney sample was performed by a pair of mirrors mounted to XY scanning galvanometers (Cambridge Technology, MA, USA) and a microscope objective.

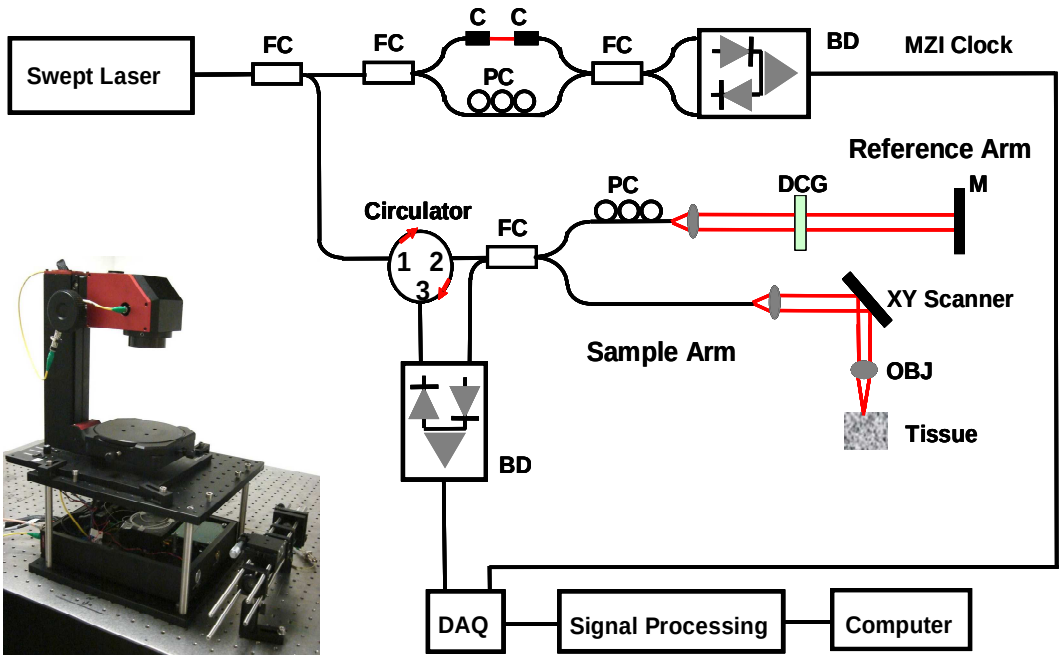

Fig. 2. Schematic and photo of the OCT imaging system. FC: fiber coupler, PC: polarization controller, C: collimator, MZI: Mach-Zehnder interferometer (frequency clocks), M: mirror, BD: balanced detector, DAQ: data acquisition board, DCG: dispersion compensating glasses, OBJ: objective.

The OCT imaging system's sensitivity was 97 dB (defined as the signal-to-noise ratio for a perfect sample reflector) [27]. 3D OCT images of the kidney measuring 3 mm by 3 mm by 2.25 mm (512 x 512 x 512 pixels) were obtained from various locations on

the human kidney samples within minutes, in a non-contact manner. The software associated with the OCT system saved each set of data as a file with extension of .IMG, which contains all information of the entire volume of images within a certain location. Images along the three orthogonal image-planes (XY, YZ, and XZ) in the Euclidean space could be extracted and displayed effectively by MATLAB routines.

After the acquisition of original images, 3D OCT images with representative microstructures were selected and compared with corresponding conventional histology. To quantitatively evaluate and classify the OCT images to obtain diagnostic information, automated image processing was performed on each individual cross-sectional (XZ or YZ plane) OCT image.

CHAPTER 3

3 IMAGE PREPROCESSING

3.1 Procedures of image processing

In disease diagnosis, most suspicious regions of OCT images have subtle abnormalities, and at the same time the OCT suffers from speckle noises. All these factors directly reduce the reliability of monitoring and diagnosing diseases. Therefore, image denoising and enhancement are the primary steps after raw images acquisition. In order to obtain valuable information from OCT, image segmentation is another important step for feature extraction or image enhancement. These steps are referred to as preprocessing. Based on the segmented images, researchers are able to perform the measurements such as characteristics quantification. Finally, image classification is necessary in certain situations, when real time monitoring and massive data analysis make it near impossible to implement manually.

In the following sections, these image processing techniques mentioned above will be reviewed in the case of human kidney images obtained by OCT. In order to prove the effects of image preprocessing, the comparison is displayed between a segmentation based on the raw image and the preprocessed image.

3.2 Image preprocessing

The image preprocessing involves image denoising, enhancement, etc to get the images ready for the next step, such as features extraction.

3.2.1 Image denoising

Denoising is noise removal while preserving as much of the significant features as possible. Speckle noise is one of the main sources of image quality degradation. Speckles arise as random interferences between reflected waves that are mutually coherent. It is one of the natural consequences of the limited spatial-frequency bandwidth of the interference signals measured in OCT [28]. The OCT speckle is similar to the speckle in ultrasound or radar imaging, which is a complex phenomenon but in general occurs when light from a coherent source illuminates scatters separated by distances near that of the coherence length of the source [29].

It is important to point out that speckle is both the signal and the noise in OCT. Thus, the objective of speckle reduction is to suppress signal degrading speckle and accentuate signal-carrying speckle [28]. In order to achieve this objective, numerous approaches have been developed, such as polarization diversity, spatial compounding, frequency compounding, and digital image processing. The most popular image processing methods are spatial filters, including mean, median, and hybrid median. Other techniques include rotational kernel transformation (RKT), Wiener filtering, multi-resolution wavelet analysis, and adaptive smoothing and anisotropic diffusion [30].

For example, in the image processing method of median filtering, the median filter replaces a pixel by the median of all pixels in the neighborhood:

$$y[m,n] = median\ \{x[i,j], w\ \ni\ (i,j)\} \qquad (1)$$

where w represents a neighborhood centered around location (m,n) in the image. One benefit of median filter is that it can suppress isolated noise without blurring sharp edges.

Many granular or mottled patterns on the image are the speckle noises which do not correspond to the real kidney microstructure, so it is challenging to detect the kidney features in the OCT images. Therefore, a 5x5 median filter was first applied to the OCT images to reduce the background speckle noise. Figure 3 is an example of filtered human kidney image obtained by OCT.

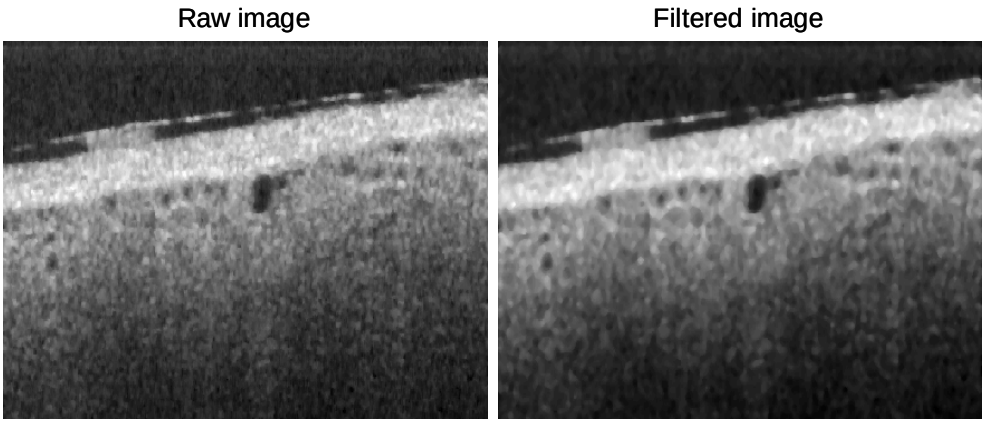

Fig. 3. OCT images of Human kidney before (left) and after (right) median filter.

3.2.2 Image enhancement

The aim of image enhancement is to improve the interpretability or perception of information in images for human viewers, or to provide better input for other automated image processing techniques. For example, image enhancement will eliminate errors caused during the image acquisition and can reduce brightness effects on the image. Typical image enhancement methods include Gamma correction, adaptive contrast enhancement, edge enhancement, and histogram equalization. Gamma correction is a nonlinear transformation process which can alter the transition from one gray level to the next, and change the contrast and latitude of gray scale in the image [31]. Histogram equalization enables the most frequent intensity values to effectively spread out, which

can increase the local contrast without changing global contrast of images. Histogram equalization is usually applied to images having backgrounds and foregrounds which are both bright or both dark. Figure 4 shows a raw image of human kidney and the image enhanced in contrast.

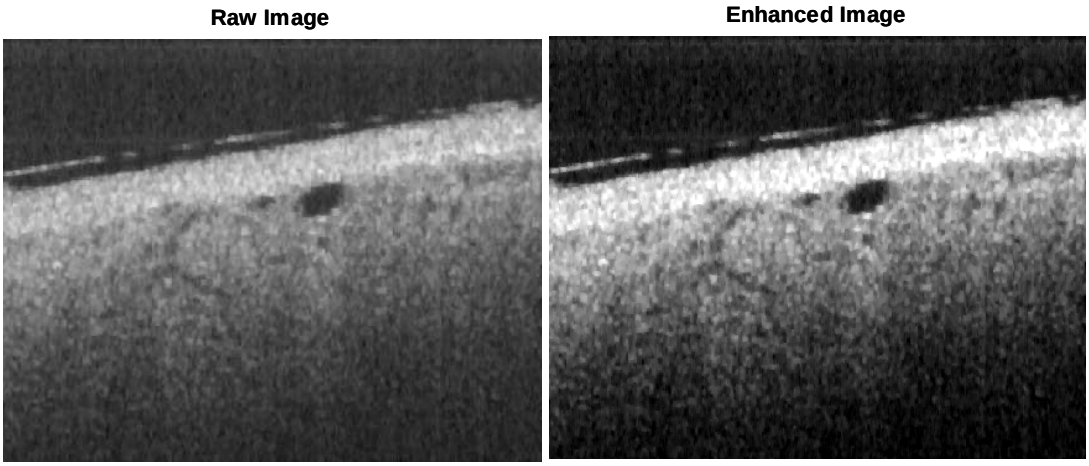

Fig. 4. OCT images of Human kidney before (left) and after (right) contrast enhancement.

3.3 Preprocessing effect

Image preprocessing is useful for subsequent operations such as segmentation. The goal of segmentation is to obtain informative image data, while avoiding pixels with noisy image data. Figure 5 is the comparison between segmented images with and without preprocessing. Compared to segmentations based on raw image, segmentations from preprocessed images are less noisy. According to the comparison from the segmentation results, it is mature to conclude that the image preprocessing does play an important role for the following image analysis.

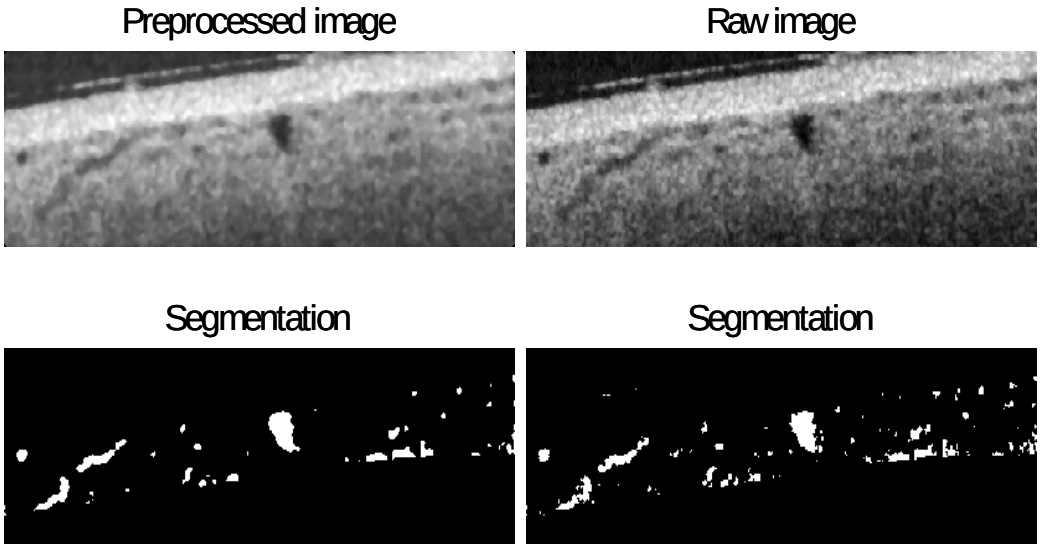

Fig. 5. Segmentation comparison between raw image and preprocessed image. Left top: image after preprocessing; left bottom: segmentation based on the preprocessed image; right top: raw image; right bottom: segmentation based on the raw image;

CHAPTER 4

4 IMAGE QUANTIFICATION AND VISUALIZATION

4.1 Image quantification process

The overall automated image quantification included image segmentation, ROI selection, and image feature quantification. Fig. 5 displays a general flow chart of the automated imaging quantification procedure.

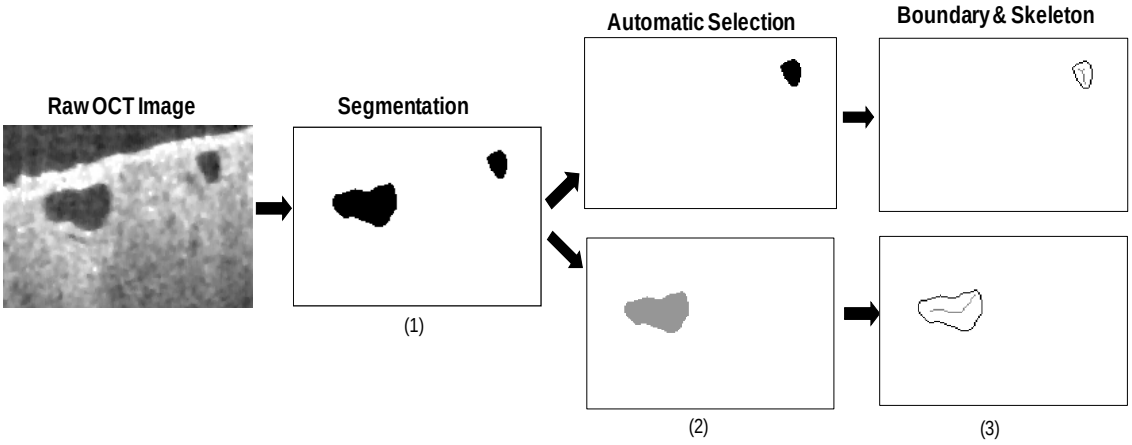

Fig. 6. General flow chart of the automated image processing algorithm, which includes three major steps: 1) image segmentation from the raw OCT image; 2) automated region selection (denoted by different gray values), enabling individual analysis of each isolated region; 3) finding the boundary and skeleton for each isolated region, and quantification of the local tubule/vessel diameters.

First, the raw image data were obtained by the OCT system and were displayed in both XZ and YZ plane. The contour of kidney surface was identified by edge detection on each A-scan. Then the structures in the kidney (such as uriniferous tubules and blood

vessels) were segmented from the kidney parenchyma based on their different backscattering intensities [23] (Step 1 in Fig. 6).

To accurately distinguish local changes, an image processing algorithm was used to automatically identify and separate the isolated sections (e.g. uriniferous tubules) from the segmented images to quantify the diameter of each ROI (such as individual tubules or blood vessels). The algorithm systematically filled the region to the section boundary and labeled each region with a unique index. This algorithm allowed different regions to be individually selected for further morphometrical analysis (for instance, quantifying the diameter) or to count the total number of isolated sections (Step 2 in Fig. 6). This step was essential to ensure that the diameters measured are from the selected ROI, therefore, can be color-coded and displayed in a spatially-resolved way.

In this chapter, the objective focuses on the quantification of tubular (or vessel) diameter. To quantify the diameter of each isolated ROI, the corresponding boundary and skeleton were generated. As a result, the diameters of each luminal position in this ROI were calculated based on the average of the shortest distances from the boundary to the skeleton. To minimize the errors due to sampling, the same analysis approaches were applied to both the XZ and YZ image cross-sections, and the final dimension was calculated by averaging the values obtained from the two cross-sections (XZ and YZ). In this way, the spatially-resolved dimensional information was obtained (Step 3 in Fig. 6) and presented in three dimensions.

4.1.1 Segmentation of hollow structures

In the area of image processing, it is essential to subdivide an image into its constituent parts to distinguish the objects of interest and the background. For intensity images formed by OCT systems, there are several popular approaches including thresholding, edge detection, and region-based techniques.

Various other techniques beside these basic segmentation methods were reported recently. For examples, Yazdanpanah et al. [32] proposed a new method to segment OCT data using a multi-phase, level-set Mumford–Shah model that incorporates a shape prior based on expert anatomical knowledge of the retinal layers, avoiding the need for training. Fernandez et al. [33] examined the application of complex diffusion filtering [34] along with coherence-enhancing diffusion filtering [35] as a tool for noise reduction, segmentation, and structural analysis in retinal OCT images. The authors proposed a model based enhancement segmentation approach by combining complex diffusion and coherence-enhanced diffusion filtering in three consecutive steps.

At present, there is no universally applicable segmentation technique that will work for all images, and no segmentation technique is perfect. The specific method chosen for the OCT images is dependent on the image itself and the information requiring extraction.

In this study, we used an intensity threshold to segment the OCT images. A resulting binary image g(x,y) is defined as [36]:

$$g(x,y) = \begin{cases} 1 ; & f(x,y) < T \\ 0 ; & f(x,y) \geq T \end{cases} \quad (2)$$

where f(x,y) was the gray level of a point (x,y) in the original OCT images. Thus the pixel (x,y) corresponding to hollow structure (such as tubules) was labeled ‘1’ in the segmented image, whereas pixels labeled ‘0’ corresponded to the background (kidney parenchyma). In such a way all pixels with a gray level lower than empirical value threshold (T) were extracted from the background for each image. Step 1 in Fig. 6 shows a typical segmentation procedure of a human kidney image.

4.1.2 Automated selection of isolated ROIs

The intensity values of the segmented images g(x,y) were scanned pixel by pixel. The background intensity was ‘0’ and each isolated ROI was ‘1’, every time a ‘1’ was detected, the program was triggered to fill the region. The filling process flooded the region in four directions (up, down, left and right) until reaching the boundary, i.e., encountering ‘0.’ The filling process was performed in MATLAB based on the function “encodem”. Fig. 7 shows the process of segmentation followed by the automated selection of individual isolated ROIs. The filling process filled different regions with different values (as indicated by different colors in Fig. 7) in order to count the regions and extract each region from the image for further processes.

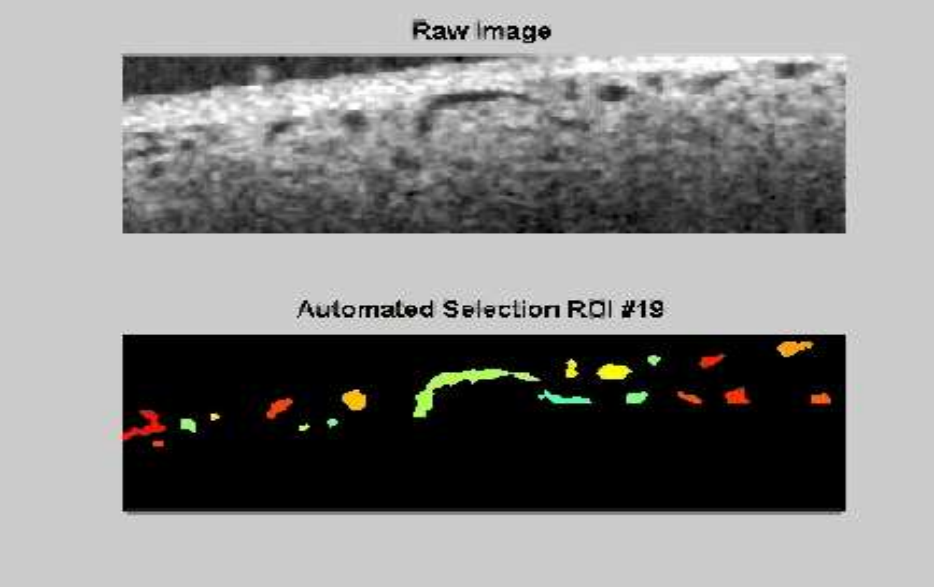

Fig. 7. Demonstration of automated selection of isolated ROIs (as indicated by different colors) (Media 1). This process enables further image analysis algorithm (such as diameter quantification) being applied to a spatially-resolved ROI instead of the whole image.

4.1.3 Quantification of image features

Quantitative analysis supplies numerical values of image feature, such as thickness, diameter, area, volume, and curvature, to assist researchers in providing correct diagnosis. Compared to manual measurements, computer-based quantitative analysis is more accurate, objective, economical, and time efficient.

Quantitative analysis also relies on morphological image processing, which is crucial for obtaining feature components that are useful in the representation and description of region shape, i.e. boundaries, skeletons, and the convex hull. The two basic morphological functions are erosion - the removal of pixels from the periphery of a feature, or dilation - the adding of pixels to that periphery. An opening is erosion followed by dilation, while a closing is a dilation followed by erosion. These operations

can smooth irregular borders, and fill in or remove, isolated pixel noise and fine lines. Because opening suppresses bright details smaller than the specified seed, and closing suppresses dark details, they are used often in combination as morphological filters for image smoothing and noise removal [36].

After extraction of an individual ROI, further morphometric analysis could be performed on the region. In the present study, we focused on the estimation of the diameter of the tubular lumen. The diameter was quantified by measuring the radius, which was the minimal distance from a specific boundary pixel to the skeleton (see Fig. 8).

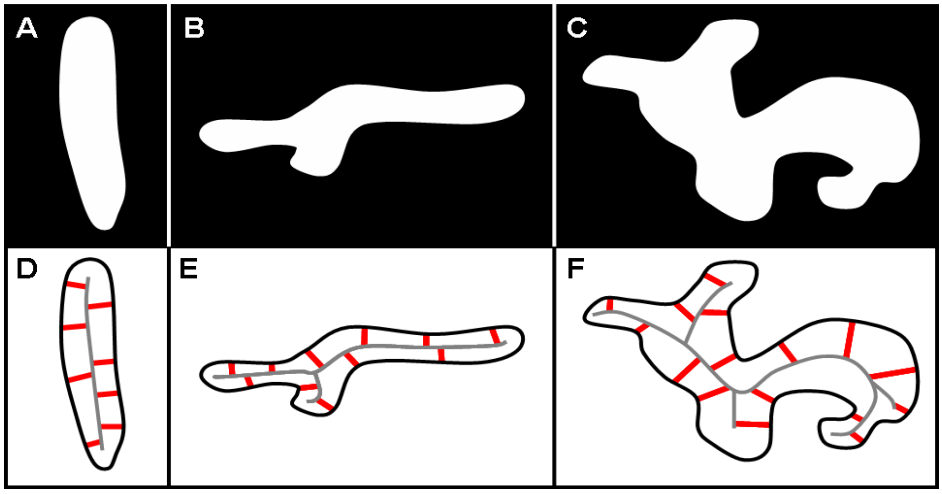

Fig. 8. Illustration of segmented image (A-C) radius quantification. D, E, and F are the graphical representations of the radius quantification of the segmented images A, B and C, respectively. A limited number of radii are shown (in red color). Boundary is shown in black color, and the skeleton is shown in gray color.

The boundary was defined as a pixel set where the spatial neighbor of every member contains both intensity ‘1’ and ‘0’ pixels. The skeleton is another pixel set which represents spatially a minimally connected stroke that a region thins to [37]. The

boundary and skeleton were obtained by the MATLAB function “bwmorph”. By using these two pixel sets, the radius for every pixel (b) on the boundary (B) was defined to be:

$$Radius\ (b) = \min_{\forall s \in S}(dist.(b, s)) \quad (3)$$

A radius was determined for every point b by finding the minimal distance between b and the skeleton set (S). This process was applied to both cylindrical and non-cylindrical structures as illustrated in Fig. 8. For visual purposes, pixels’ intensities were rendered with a number twice that of the associated radius (the local diameter of the feature).

4.2 Results

4.2.1 Calibration of the quantification algorithm

To quantitatively assess the accuracy of the dimension calculation algorithm, we applied this algorithm to the dimensional calculation of a capillary tube phantom. By comparing the computer calculated results with manual measurements, the performance of the algorithm was validated.

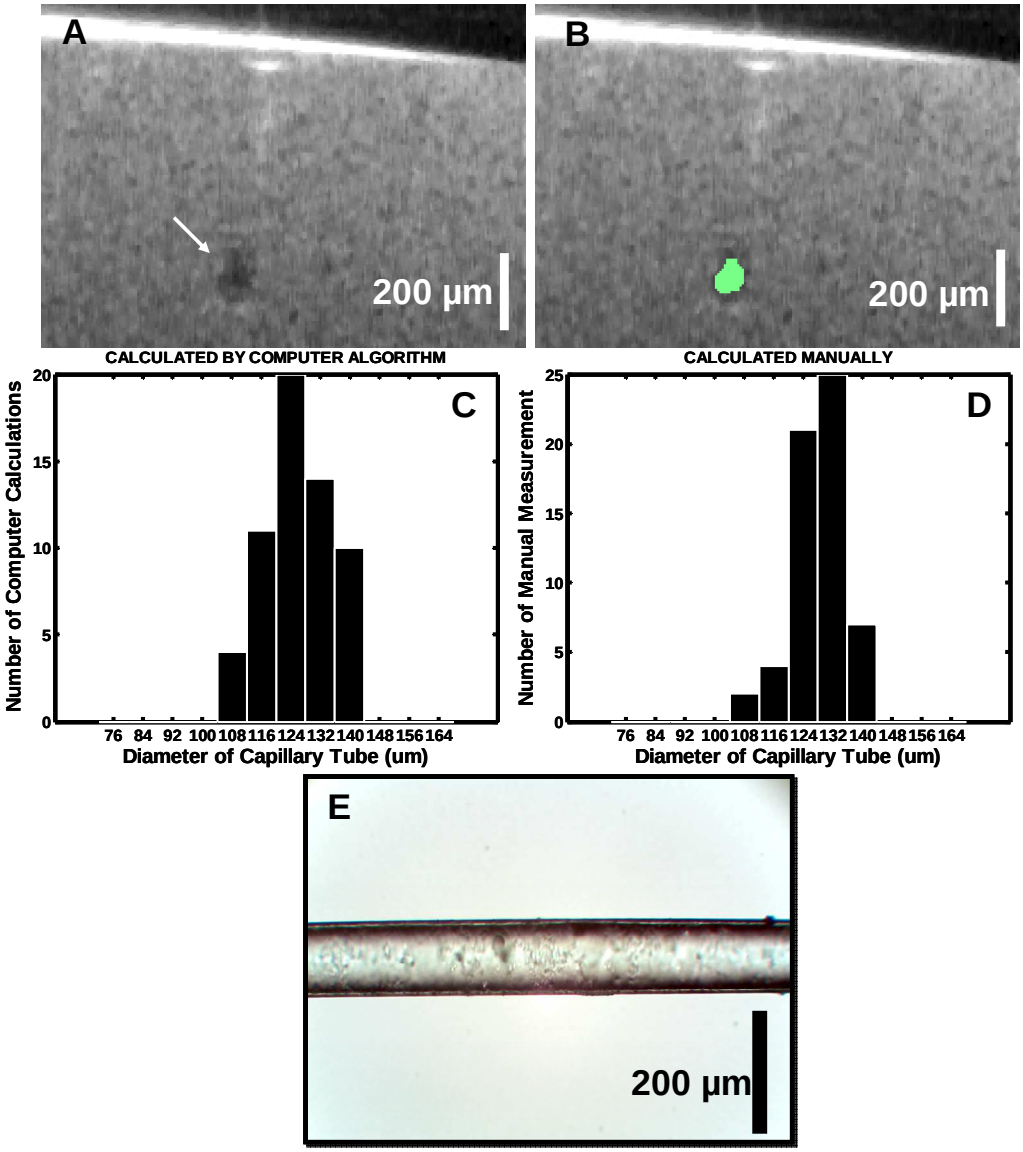

Fig. 9. (A) An OCT image of a capillary tube phantom in YZ plane. The tube (indicated by an arrow) is submerged in a highly scattering medium with 2% Intralipid (a safe fat emulsion for human use). (B) Corresponding segmentation image of (A). Tube region is highlighted by green color. (C) Histogram of the estimated tube diameters from 61 different OCT cross-sectional (YZ) images along X dimension by computer analysis and a human observer (D). (E) A digital microscopy image of the capillary tube.

Fig. 9A shows one representative cross-sectional OCT image (YZ) of a capillary tube phantom, with the associated segmented image shown in Fig. 9B. Fig. 9C shows the histogram of the automated estimation of the tube radius from a total of 61 different YZ cross-sectional OCT images along X axis. The computer algorithm estimated the diameter of the capillary tube to be 126.6 ± 8.6 μm. A human observer measured the diameter directly from the same set of OCT images, and result in 128.3 ± 7.4 μm (Fig. 9D). The computer analysis result shows a slightly larger variance since the diameter is averaged from all boundary pixel measurements, while the human observer only selected few edge pixels to quantify the diameter. Fig. 9E shows a digital microscopy image of the capillary tube. The measured diameter is 132.7 ± 0.9 μm.

The relatively larger standard deviation from the computer algorithm compared to digital microscopy is due to: 1) the OCT imaging of tube phantom (containing the scattering media) has lower contrast compared to digital microscopy imaging of tube in air; 2) OCT imaging system has lower resolution (10 μm) compared to that of digital microscopy (~1 μm). Therefore, the tube edge in OCT image is not as sharp as those in the digital microscopy, which will result in errors in segmentation. Nevertheless, the result shows that the mean of estimation obtained by the automated computer analysis is comparable to the true tube dimension.

4.2.2 Comparison between OCT imaging and histology

The kidney microstructures of interest, including the uriniferous tubules, vessels, and glomeruli were identified based on their distinct morphologies. Comparisons between the OCT image and the corresponding histological micrograph indicated a close match in terms of the main structural features. In addition, the resolution of the OCT

images (~10 µm) was sufficient for the purpose of revealing the morphological details. Fig. 10A shows a representative cross-sectional OCT image of the human kidney, and Fig. 10B is the corresponding histopathology.

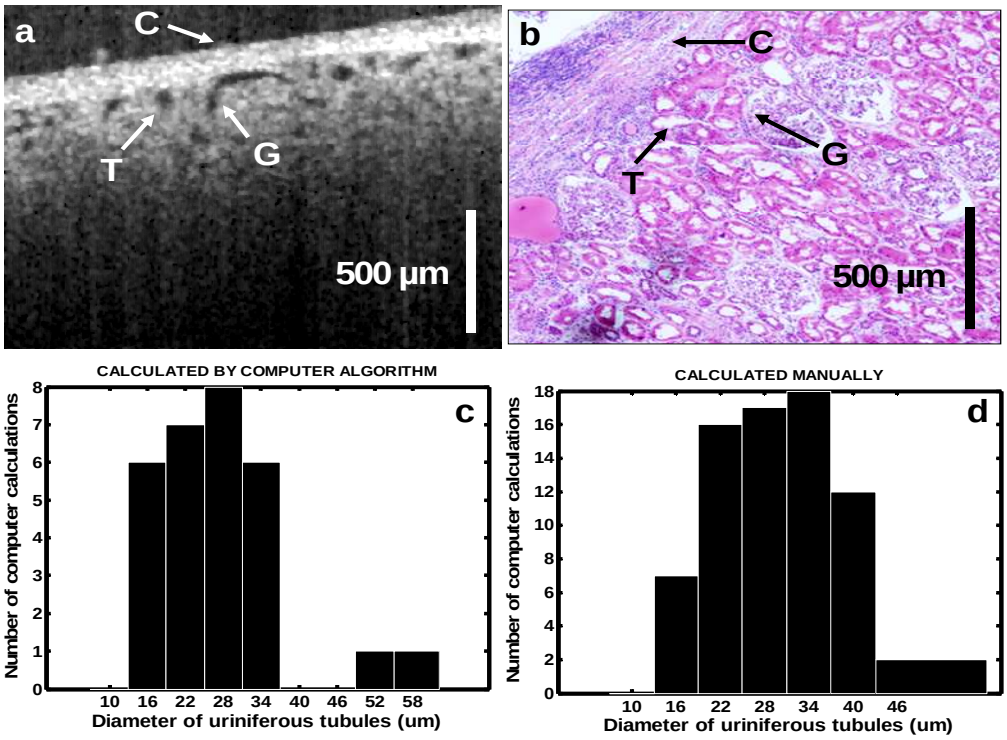

Fig. 10. (a) Cross-sectional OCT image of the human kidney. Uriniferous tubules (T), glomerulus (G) and the kidney capsule (C) are distinguishable. (b) Conventional histology of the associated area in the human kidney. (c) and (d) are the histograms of the uriniferous tubules diameters calculated by the computer algorithm from OCT images, and manually measurement from the histology, respectively.

As seen in Fig. 10A, tissues with high backscattering such as kidney capsule appeared bright, while low backscattering regions such as uriniferous tubular lumens appeared dark. It was clearly observable that OCT could penetrate through the kidney capsule (C) with a penetration depth of more than 800 µm. The kidney microanatomy including uriniferous tubules (T) and glomeruli (G) were also readily distinguished.

Fig. 10C shows the histogram of the tubular lumen diameter measured by the automated algorithm described in Section 2.3. Automated measurement gives an

estimation of lumen diameter of 27.5 ± 10.1 µm. The manual measurement of lumen diameter from the histology slide (Fig. 10B) gives the results of 29.5 ± 9.2 µm (see Fig. 10D). This shows that the results obtained by the automated computer analysis are comparable to that of the manual measurements of histology slide. However, the computer calculation was significantly faster than the manual measurements. In addition, computer-aided analysis promises to automatically analyze a large volume of data (for example, three-dimensional data) efficiently and will be very helpful for providing the clinicians with quantitative information in a timely manner.

4.2.3 Quantification and three-dimensional imaging visualization

4.2.3.1 Human kidney case I (blood vessels)

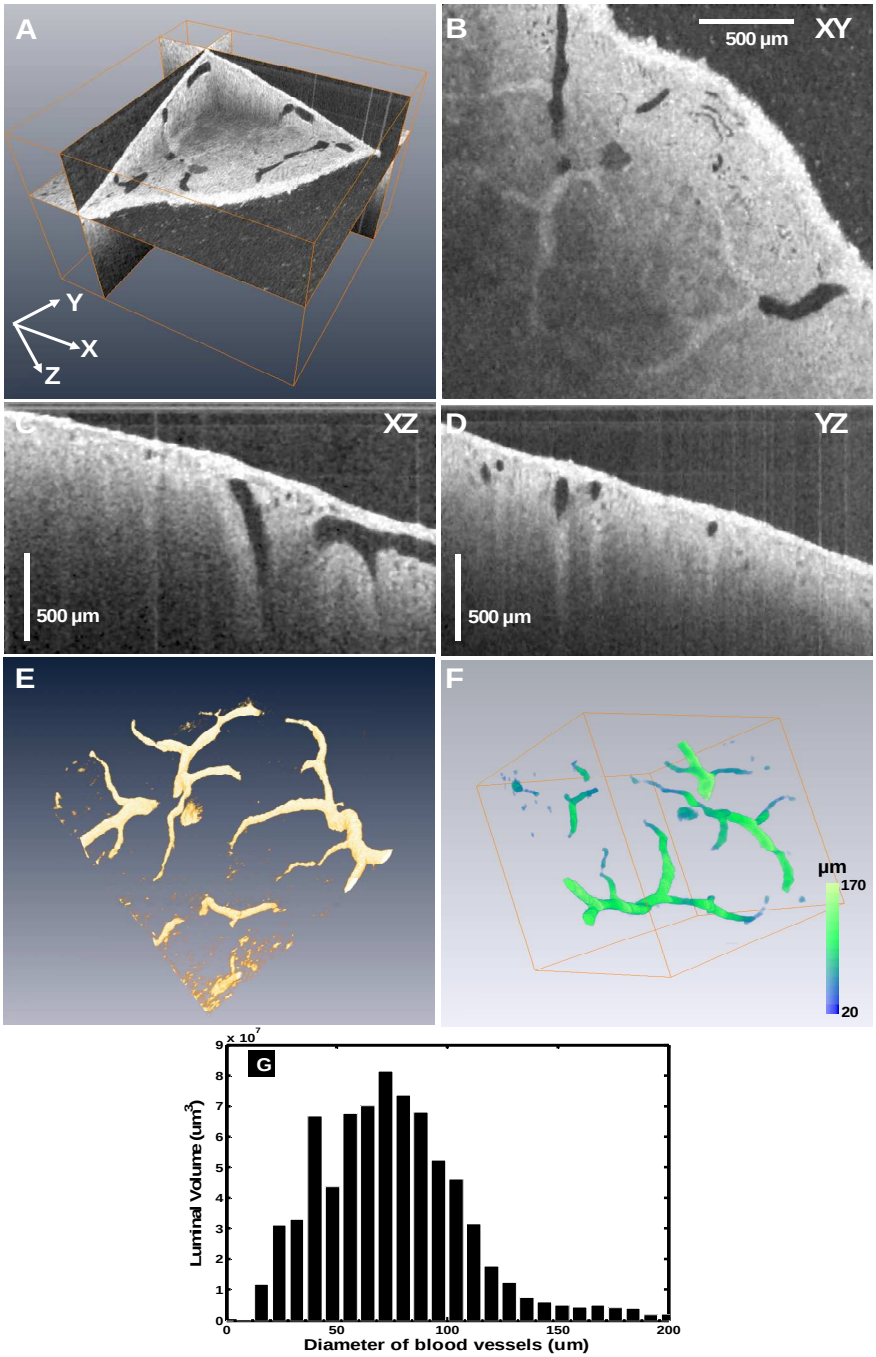

Fig. 11. (A) 3D cut-through view of the human kidney. The blood vessels as well as the kidney parenchyma are visualized. (B-D): Representative OCT images in the XY, XZ, and YZ planes. (E) 3D volumetric image of the segmented vasculature (Media 2). (F) Automatically quantified and color-coded structural image. (G) Volume histogram of the blood vessel diameter distribution.

Fig. 11A is the three-dimensional view of the human kidney, as generated from individual cross-sectional images. Fig. 11B-D shows representative images along the three orthogonal planes (XY, YZ, and XZ), respectively. Detailed kidney vascular networks were visualized in all the image planes. The OCT image data set was further segmented and analyzed to quantify the luminal diameter of the blood vessels. Fig. 11E shows the 3D reconstructed images showing vascular trees after intensity segmentation. The segmented 3D vascular tree was reconstructed by utilizing a 3D visualization software (Amira). The morphological features of the blood vessels can be examined. Fig. 11F shows the quantification of the representative blood vessels luminal diameters from the ROI. Fig. 11G shows the volume histogram of the diameter (which is obtained by counting the voxel numbers associated with the specific diameter, and multiplied by the individual voxel volume, 150.9 μm^3), indicating that the majority of vessel diameters range from 50 μm to 100 μm.

For those regions without any microstructures such as tubules or vessels, the light intensity decreases exponentially with depth because of light scattering effects. However, hollow microstructures such as uriniferous tubules or blood vessels alter this exponential decay pattern due to the minimal light scattering within these hollow structures. After the light passes through these structures, it continues decreasing again. This phenomenon results in relatively higher light intensity (hyperdense shadow) below some of the microstructures as shown in the cross-sectional images (Fig. 11C and D), and casts white shadows on the enface image (Fig. 11B).

4.2.3.2 Human kidney case II (uriniferous tubules)

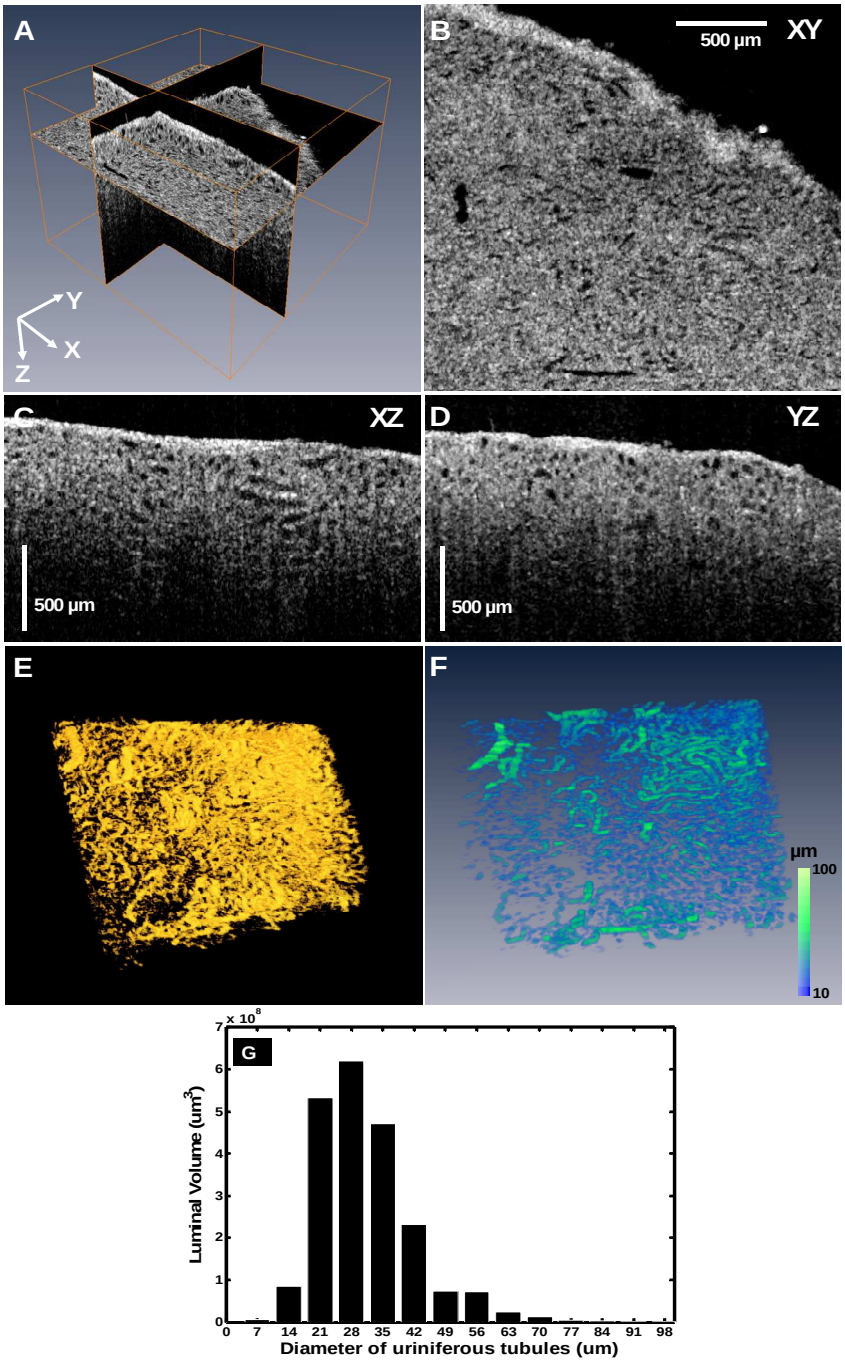

Fig. 12. (A) 3D cut-through view of the human kidney including uriniferous tubules and the kidney parenchyma is displayed. (B-D): Representative OCT images in the XY, XZ, and YZ planes. (E) 3D volumetric image of the segmented tubular network (Media 3). (F) Automatically quantified and color-coded structural image. (G) Volume histogram of the uriniferous tubules diameter distribution.

The previously described procedures were applied to another kidney as shown in Fig. 12. As with case I, detailed kidney tubular structures were visualized in all image planes (Fig. 12A-D). Fig. 12E shows the 3D reconstructed images of the tubular network after intensity segmentation, which allows comprehensive examination of morphological features and interconnectivity of the renal tubules. Fig. 12F shows the automated quantification of tubular diameters, which were color-coded on the structural map. The volume histogram in Fig. 12G indicates that most tubule luminal diameters at this region range from 20 µm to approximate 40 µm, with a mean diameter around 30 µm.

4.2.3.3 Human kidney case III (distended uriniferous tubules)

Case III is from a third kidney. Fig. 13A-D show the 3D cut-through views and the representative images along the three orthogonal planes. Two clusters of distended tubules are clearly identified on Fig. 13E. Fig. 13F shows the automated quantification of all the luminal tubular diameters. The tubular lumen diameters range approximately from 30 – 60 µm in diameter, as shown in the volume histogram (Fig. 13G).

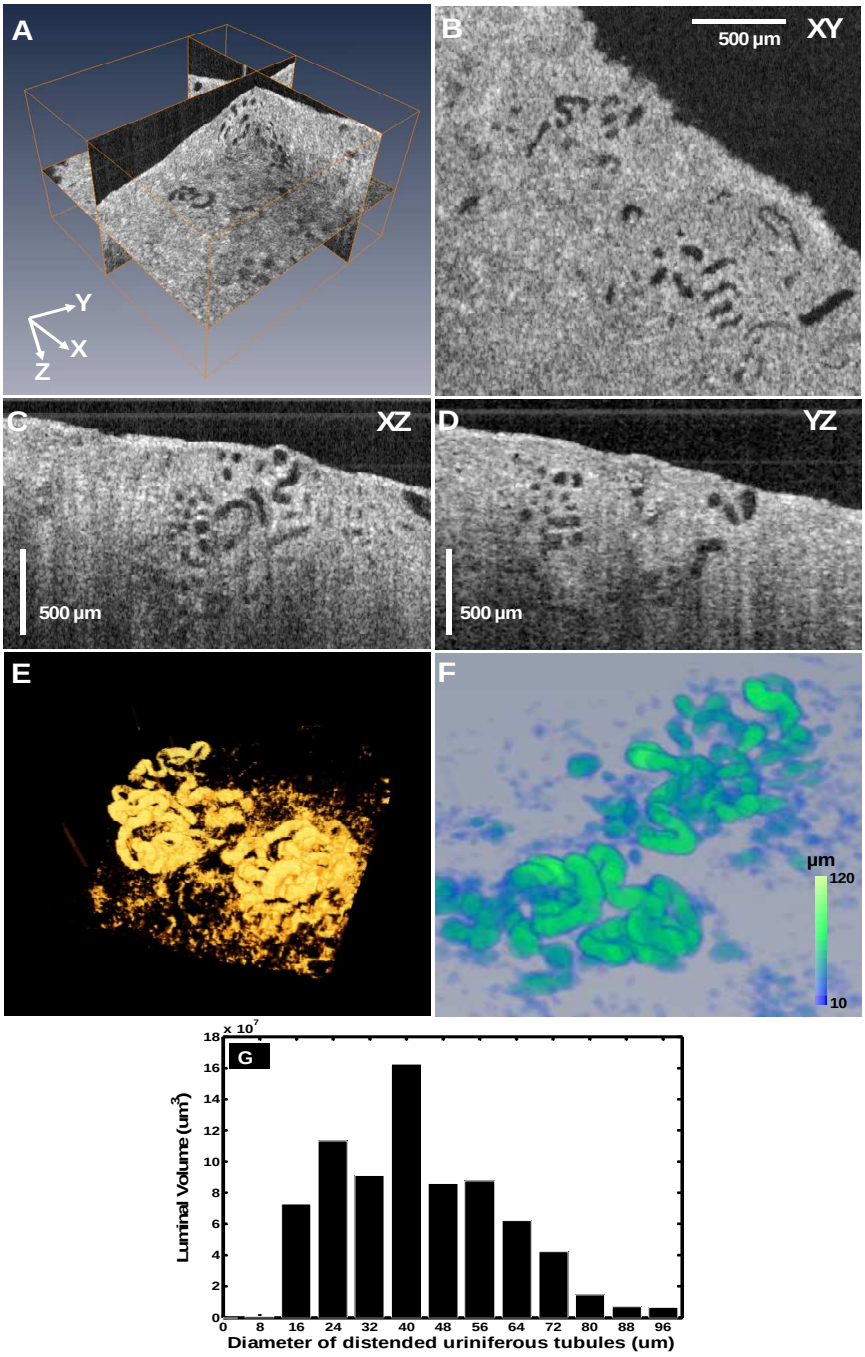

Fig. 13. (A) 3D cut-through view of the human kidney with distended uriniferous tubules. (B-D): Representative OCT images in the XY, XZ, and YZ planes. (E) 3D volumetric image of the segmented distended tubular network (Media 4). (F) Automatically quantified and color-coded structural image. (G) Volume histogram of the distended uriniferous tubules diameter distribution.

Based on the volume histograms of blood vessels, distended tubules, and uriniferous tubules, the comparison among three different microstructures is shown in figure 14. The peaks of the dimension distributions are significantly different in terms of the histogram showed in fig. 14.

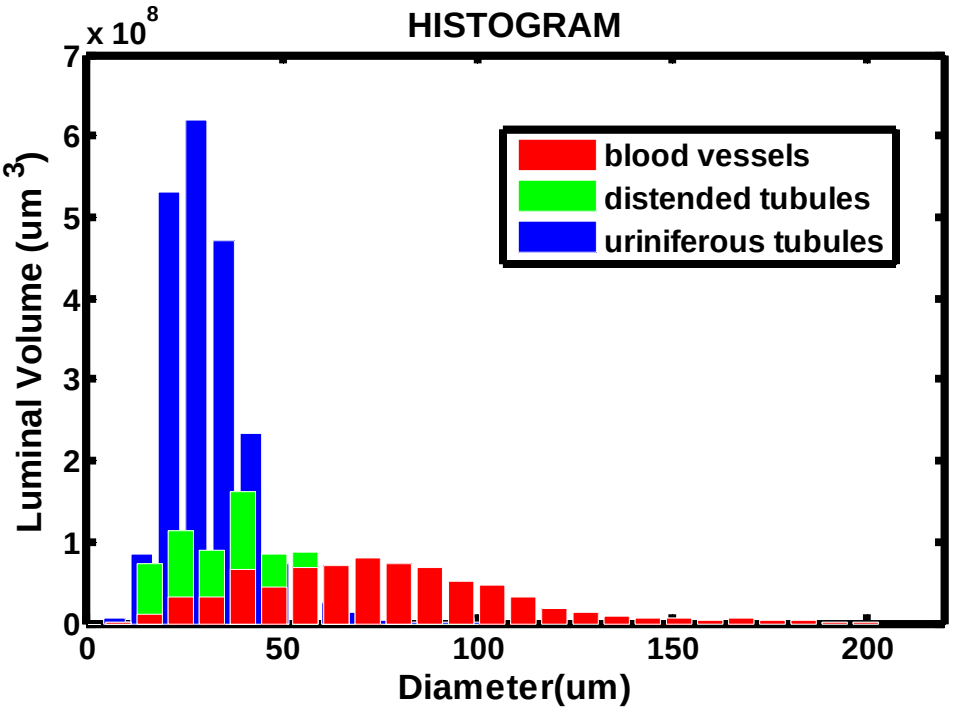

Fig. 14. The histogram of luminal Volume distribution for blood vessels (red), distended tubules (green), and uriniferous tubules (blue).

4.2.3.4 Human kidney case IV (glomerulus)

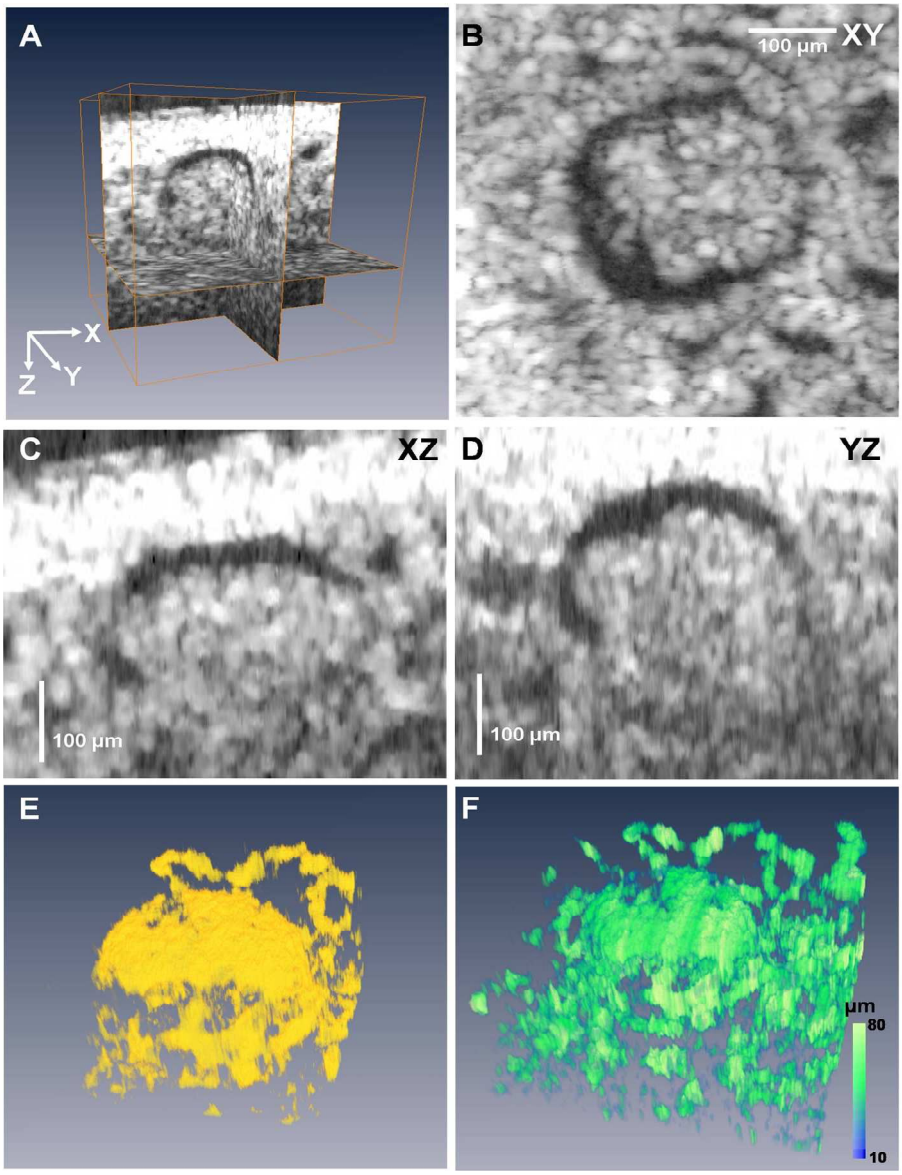

Fig. 15. (A) 3D cut-through enlarged view of the human kidney showing a glomerulus and tubular network. (B-D): Representative OCT images in the XY, XZ, and YZ planes. (E) 3D volumetric image of the segmented glomerulus and tubular network (Media 5). (F) Automatically quantified and color-coded structural image.

We were also able to visualize the glomerular structures. Fig. 15A-D shows an individual glomerulus in the enlarged view, as compared to previous figures. We could

easily visualize the glomerulus surrounded by the circular Bowman's space. However, the segmentation of the complete glomeruli was challenging, because in most cases, the Bowman's space separating the glomerular capillary tufts from the renal parenchyma is not a full circle (see Fig. 15D and Fig. 15B). Fig. 15D shows the diameter of the glomerulus to be approximately 220 μm. This result is in agreement with previous literature using ultrasound imaging (216 ± 27 μm) [38]. Fig. 15E shows the 3D view of the segmented Bowman's space.

4.2.3.5 Human kidney case V (vessels, tubules, & glomeruli)

Fig. 16 shows a representative region with different renal structures including blood vessels, uriniferous tubules, and glomeruli. The glomeruli are surrounded by an expanded network of uriniferous tubules and blood vessels. The diameters of the glomeruli are approximately 200 μm. This result demonstrates the capability of OCT to visualize different renal microstructures *in situ*.

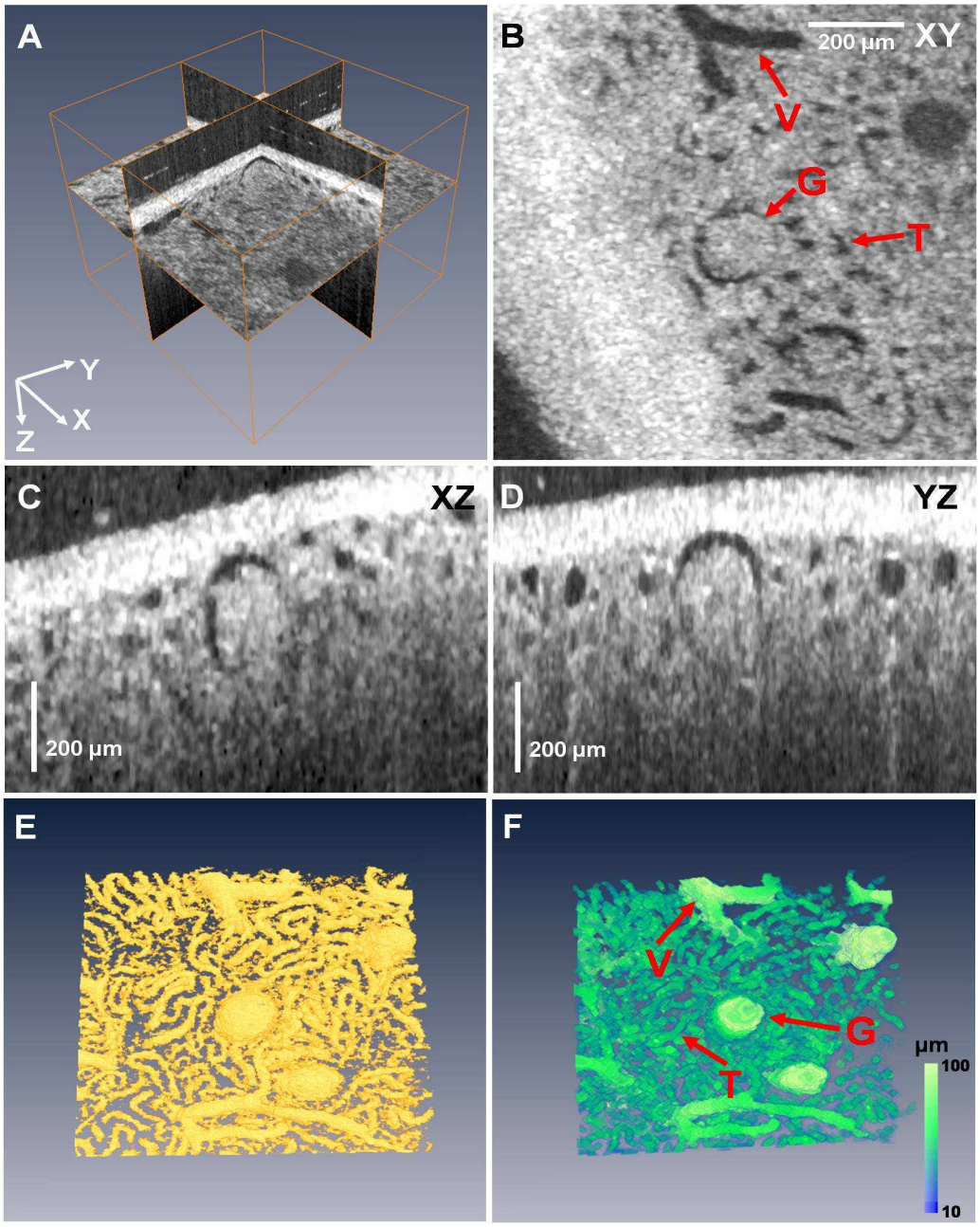

Fig. 16. (A) 3D cut-through view of the human kidney showing a glomerulus (G) surrounded by tubules (T) and vessels (V). (B-D): Representative OCT images in the XY, XZ, and YZ planes. (E) 3D volumetric image of the segmented glomeruli and tubular network (Media 6). (F) Automatically quantified and color-coded structural image.

CHAPTER 5

5 IMAGE CLASSIFICATION

5.1 Classification definition

An object is a physical unit, usually represented in image analysis by ROIs in segmented images [39]. The set of objects can be divided into disjoint subsets, which have some common properties and are called classes. Classification aims to classify data based either on a priori knowledge or on statistical information extracted from the patterns. The patterns to be classified are usually groups of objects from images to be analyzed.

The main image classification steps are in shown in figure 17 [39]. The block ‘Construction of formal description’ is based on the experience and intuition of the designer. A set of elementary properties is chosen which describe some characteristics of the objects; these properties are measured in an appropriate way and form the description pattern of the object. These properties are defined as descriptors and can be either quantitative or qualitative in character. A classifier places patterns into a specific class based on these descriptors of the pattern.

Mathematically the approaches to image classification are divided into two principal areas: decision-theoretic and structural [36]. The first category deals with patterns described using quantitative descriptors, such as length, area, and texture. Sonka et al. [39] listed some simple geometric region descriptors: Area, Euler’s number, projections, height, width, eccentricity, elongatedness, rectangularity, direction and

compactness. The second category takes use of structural relationships inherent in a pattern's shape, which seek to achieve pattern recognition by capitalizing precisely on these types of relationships.

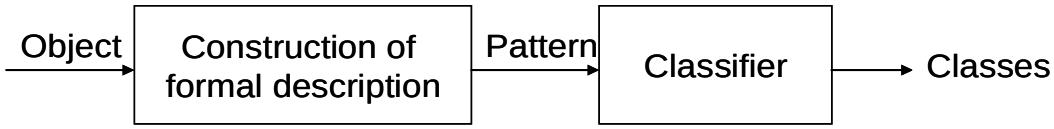

Fig. 17. Main steps of image classification.

Image classification helps biochemists, biologists, medical scientists, and physicians to judge quantitative measurements, which facilitate the validation of scientific hypothesis and accurate medical diagnosis. Image classification is also the basis for computer-aided diagnosis systems in medical-imaging-based diagnostics areas.

5.2 Kidney image classification algorithm

Decision-theoretic classification is used widely in OCT image processing. Sabeenian et al. [40] found out the abnormalities of a patient's abdomen and more particularly in organs such as kidney, liver, and spleen by analysis and classifying the CT scan images of a patient's abdomen. The classification is done automatically by extracting the statistical and spectral characteristics. The similar classification method is also suitable for OCT scan images of human kidney.

In the image classification for this study, the object is the isolated ROIs of a set of kidney images obtained by OCT (i.e. 512 images in XZ). The construction of formal description in current study is image grouping. Then decision-theoretic classifier is applied to each image group to estimate which class this group belongs to. The classifier works on multiple-parameter descriptors: the shape of the images and the diameters of

images. Decisions are made by priori knowledge, that is, groups with 'ring' shapes are classified to glomeruli; groups without 'ring' shapes are categorized to sclerous glomeruli, blood vessels, or tubules based on the statistical value of their diameters.

After the accomplishment of image classification, each ROI is categorized to one of the three main microstructures in the human kidney: glomeruli, blood vessels, and tubules. Figure 18 depicts the general structure of the flow chart for the classification process. T1 and T2 are thresholds derived from statistical diameter values to distinguish the class of each group. The determinate value of T1 and T2 will be discussed in the posterior sections in this chapter.

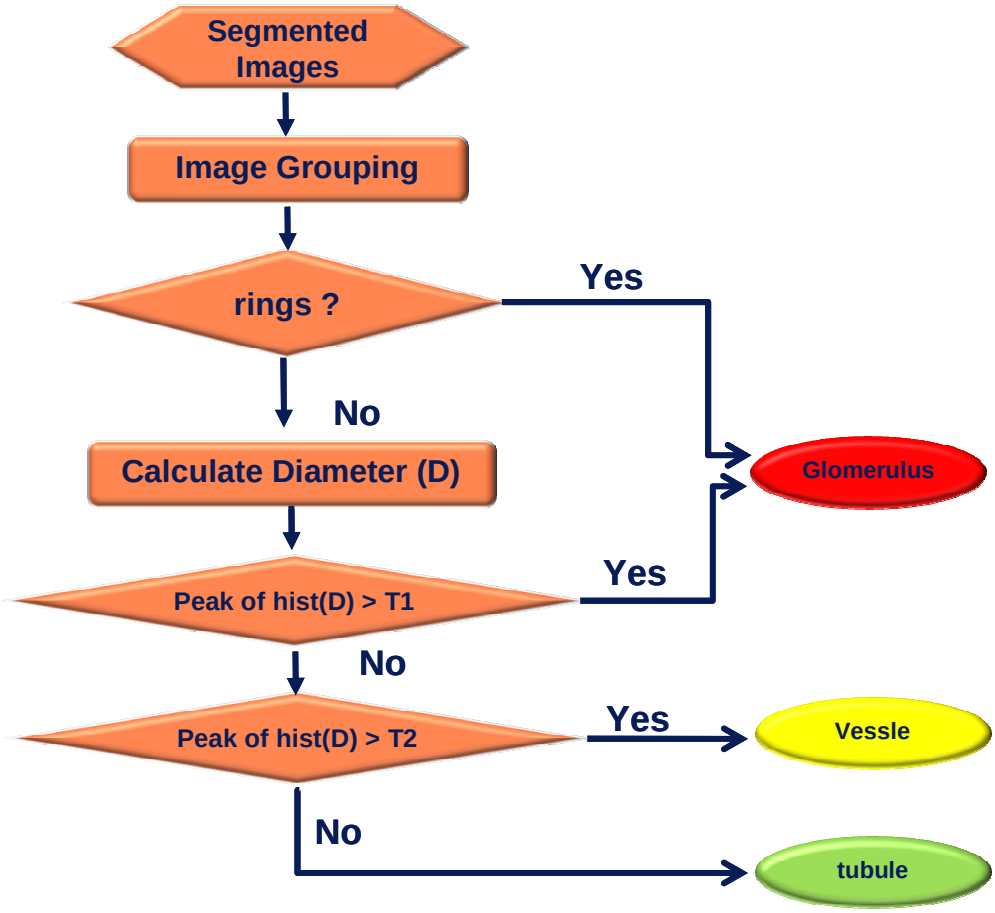

Fig. 18. Flow chart of the human kidney image classification algorithm. hist(D) means the histogram of diameter; T1, T2 are empirical thresholds.

5.2.1 Image grouping

Image grouping designates each ROI to a specific group which represents a connected entity in geometry in the human kidney.

The image grouping algorithm is fulfilled by MATLAB routines and composed of three steps: labeling, overlapping assessing, and group marking. The algorithm for labeling was the same as the ROI selection algorithm used in image quantification discussed in previous chapter. The process is to assign a unique number to each ROI of 512 images in the entire set of XZ images. The next step is to assess the overlapping of a paired ROI between two spatially consecutive XZ images. The criterion of overlapping relies on the fact that there is at least one pixel overlapped within the two ROIs. Paired ROIs unsatisfied with the criterion indicate that the two ROIs are spatially isolated. Then the program proceeds to assess the overlapping of the next paired ROIs. If the paired ROIs are overlapping, indicating that this pair represents the same entity, the program triggers the group marking process before proceeding to the next assessment. Triggered group marking program places a group marker for overlapped ROIs. The 3-step process is implemented in each ROI individually, and after the image grouping is finished, ROIs with the same marker represent that they belong to one group, in other words, one connected entity.

5.2.2 Classifiers

In this study, we are interested in three main classes in human kidney images: glomeruli, blood vessels, and tubules. The final aspect of image classification is to evaluate the class for each group. The difference among the three classes can be determined by priori knowledge: normal glomeruli have ‘ring’ shape or partial ‘ring’

shape. Sclerous glomeruli, blood vessels, and tubules only have solid disk shape or arbitrary shape. In that case, the quantification of the diameter for these three microstructures is statistically significant. As a result, the histogram distribution of the diameter values could be plotted and empirical thresholds are set to determine the class for each group. Therefore, the classifiers are made dependent on multiple-parameter descriptors: the shape of the images and the diameters of images.

First the shape classifier singles out groups which have partial-ring or ring-shape images and categorize these groups as the glomeruli class; then the left groups are estimated by the diameter classifiers and finally categorized as corresponding classes.

5.2.2.1 Shape classifier

Fig. 19 demonstrates the steps of how the shape classifier works. As shown in this figure, images from one group are severed as an input of the classification. In order to evaluate the ring-shape images in each group, a method known as ‘stable-centre’ was developed. This method is based on the assumption that any ring-shape or partial ring-shape image has a relatively fixed centre. The center coordinates (x,y) of the ring are computed by least squares means for each image within one group, and the standard deviation (STD) of the coordinates are compared by threshold t. Either STD(x) or STD(y) less than t means the images contains ‘ring’ or ‘partial ring’ shape, thus the whole group is classified as glomeruli class.

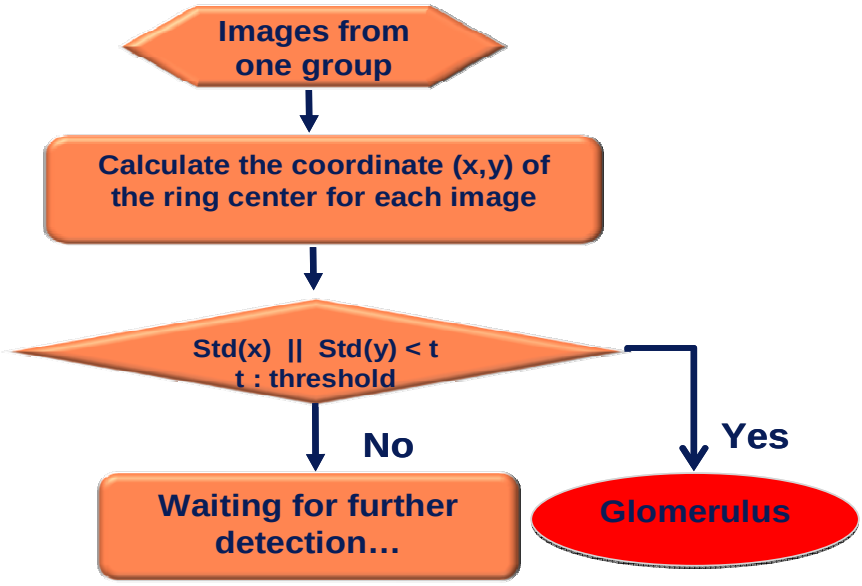

Fig. 19. Flow chart of the shape classifier. t is empirical thresholds

Shape classifier selects groups containing 'ring' or 'partial-ring' images, which is a typical characteristic of normal glomeruli, and labels the groups with a glomeruli marker. In this study, the glomeruli marker is red color.

5.2.2.2 Diameter classifier

The diameter distribution was obtained by the quantification algorithm in chapter 4. Prior knowledge shows the mean diameter of sclerous glomeruli, blood vessels, and tubules to be approximately 160 µm, 85 µm, and 30 µm respectively. Fig. 20 illustrates the difference among the three structures. The determinate values of T1 and T2 therefore can be derived from the fig. 20 distribution. At the aid of threshold T1 (120 µm) and T2 (50 µm), sclerous glomeruli, blood vessels, and tubules are separated and classified to corresponding classes.

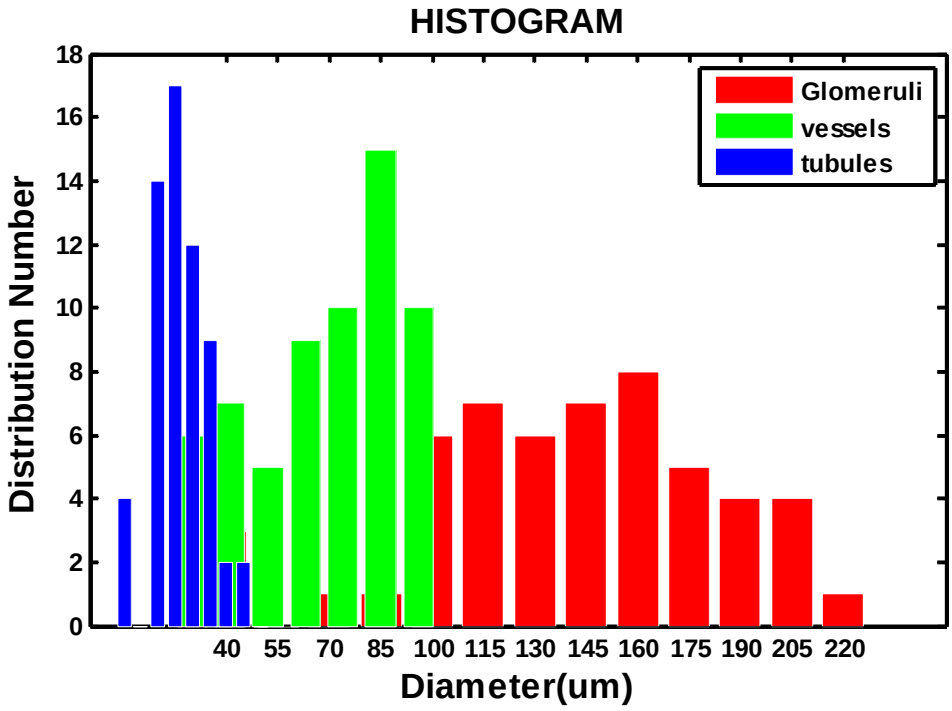

Fig. 20. Illustration of the diameter distribution for sclerous glomeruli, blood vessels, and tubules.

5.3 Results

5.3.1 Image grouping

The upper left image on Fig. 21 shows the overall image group from one human kidney sample. The other images in this figure are of selected groups from this overall image.

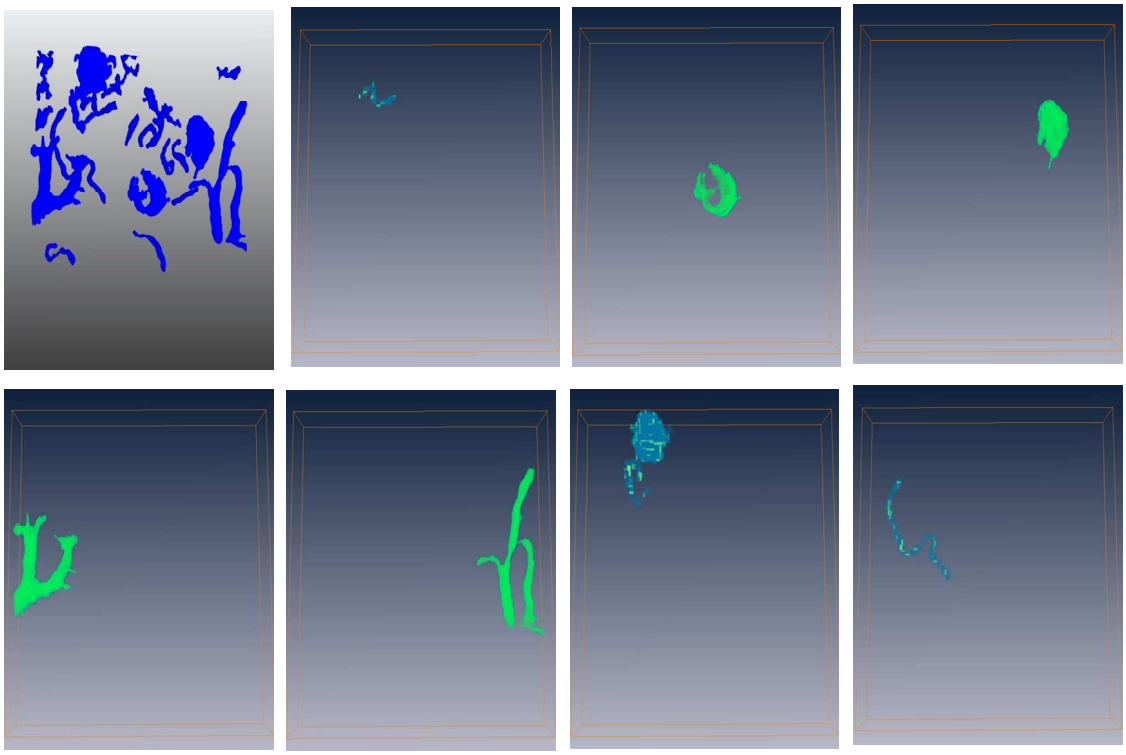

Fig. 21. Demonstration of human kidney image grouping. Top left: all groups from one human kidney sample. Others: selected groups from image grouping.

5.3.2 Image classification

Three main classes of human kidney microstructures are color coded in the Fig. 22. The red images represent glomeruli, the yellow images represent blood vessels, and the blue images represent tubules. All groups are clearly classified in this set of data.

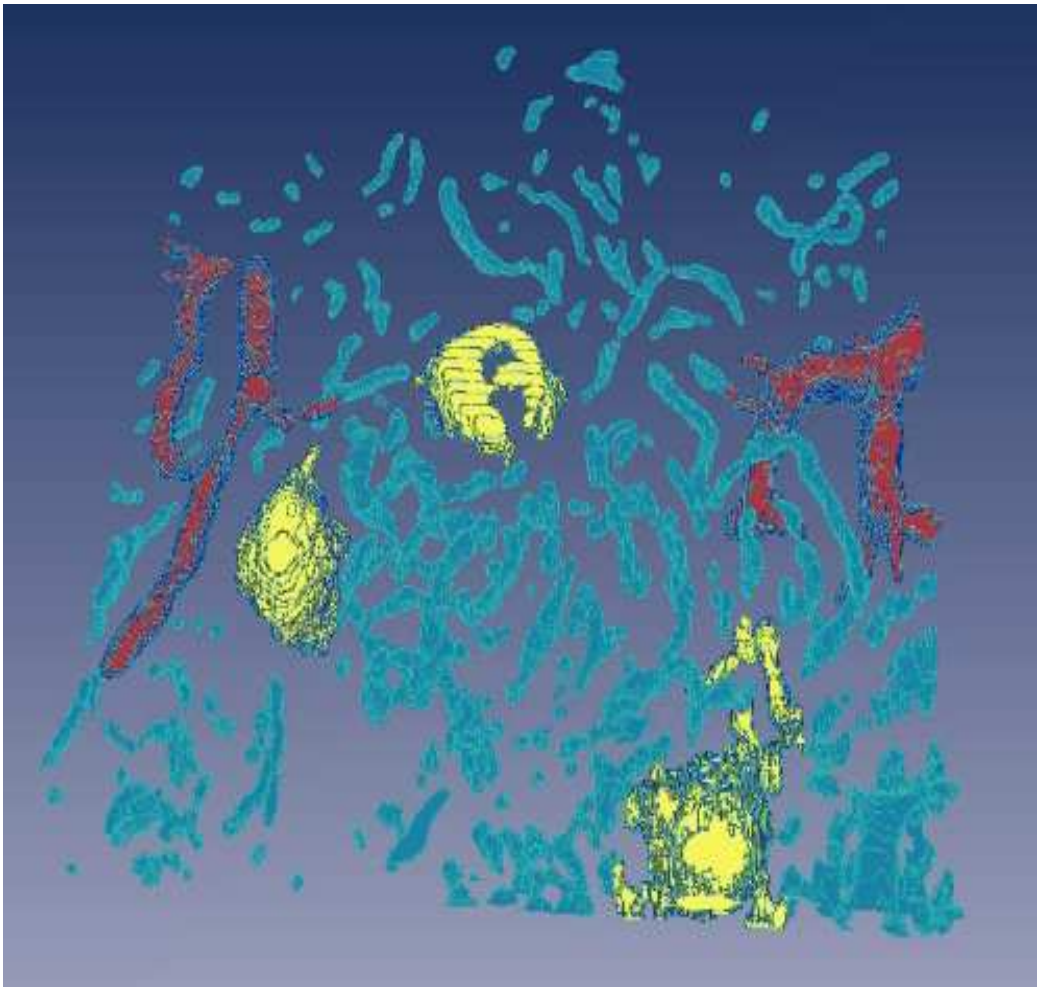

Fig. 22. Result of human kidney image classification (Media 7). Yellow: glomeruli; Red: blood vessels; Blue: tubules

Most microstructures in Fig. 22 are correctly classified and color coded according to prior experience. There is a minor error in the glomeruli class: some tubular structures were classified as the glomeruli class near the top of the figure. The reason for this error can be explained by the fact that the glomerulus and tubules are physically connected based on the segmentation information. An optimization in image segmentation and image grouping will assist in resolving this issue.

CHAPTER 6

6 DISCUSSION AND FUTURE WORK

6.1 Discussion

OCT as a high-resolution medical imaging modality has become one of the most important visualization and interpretation methods in biology and medicine. In the past decade, tremendous improvements have been accrued for OCT in both hardware and software. High speed, high resolution OCT systems have led to a rapid growth in the application of digital processing techniques for solving medical problems. A large volume of images requiring processing poses a challenge to the efficiency of today's image processing algorithm, but this can be overcome as more efficient algorithms are developed. Furthermore, as the image capturing hardware and software improves, we can obtain higher resolution images. These higher resolution images will provide us with finer image details, thus leading researchers to developing and improving their image processing techniques.

In this study, we were able to image up to approximately 800 µm depths in the human kidney, which was deep enough to image superficial blood vessels, uriniferous tubules, and glomeruli. Such structures are closely related to many physiological functions, for example, in the case of evaluation of transplant kidney function [17]. High acquisition speed (video rate) achieved by Fourier domain OCT enables real time imaging in 3D [41-44] and the surveying of large kidney surface area in a timeframe

reasonable for clinical practice. In general, with further development, OCT has the potential to be translated into clinical settings for kidney imaging.

The algorithms applied in this study, such as, automated imaging quantification and classification methods, could be generalized to many other imaging analyses. The dimensional calculation of a capillary tube phantom proved that the algorithm could successfully estimate actual luminal volumes. 3D visualization and volumetric rendering provided quantitative evaluations of the dimensional changes in tubular or vessel lumens. These renderings and the use of color coded 3D images can potentially provide clinicians with useful diagnostic tools.

However, there is still space for improvement of the current study. The first problem encountered by OCT is speckle noise, which is a never ending issue requiring extensive research for its full understanding. Noise obscures the original images, and introduces artifacts, resulting in obstructing in further operations including image segmentation and feature extraction. Certain issues are listed below which require special attention:

1. The comprehension of the types of speckle and the origin of speckle is not clear to date. Further studies are necessary to understand the relationship between the scattering properties of tissue at the microscopic level, and the statistical properties of speckle in OCT image.
2. As a natural result of the limited spatial-frequency bandwidth of an interferometric system, speckle effects in OCT should be surpassed by the way of widening the light source bandwidth and widening the light collection aperture at the same time.

3. More research is needed focusing on techniques to relate spatial-compounding and frequency-compounding methods, particularly methods used in those relatively mature techniques such as synthetic-aperture radar and medical ultrasound and how they relate to OCT.

It should also be mentioned that there are challenges in image segmentation. An intensity-based segmentation algorithm was used in this study, which is subject to the setting of threshold values. In the future, more advanced segmentation algorithms, such as marker-controlled watershed segmentation [4], will be investigated as well.

The automated selection of individual ROI for further analysis represents a unique merit of this algorithm. This approach simulates human behavior using an automated computer algorithm. After automated selection, various morphormetric analyses could be applied to the selected ROI, including the measurement of area, diameter, and curvature. In this study we focused on the local diameter because it is closely related to the kidney viability [17].

The quantification of tubular (or vessel) diameters was achieved by automated identification of the boundary and skeleton of individual ROIs. This approach was limited in its estimation of the correct tubular diameter when the imaging plane did not cut through the central axis of the tubules. However, this limitation was also shared by most, if not all, cross-sectional imaging methods. For example, histology analysis of tubular and glomeruli diameter will be subject to the same sampling limitations. In our study, 3D OCT images with two orthogonal cross-sections (XZ and YZ) were utilized to obtain an averaged estimation of the tubular dimension. The sampling limitation will be further alleviated by panning the imaging plane 180 degree to fully cover the different

angles. In addition, the skeleton extraction method used in this study is based on morphological thinning, which sometimes led to unwanted branches [4], which tended to under-estimate the tubular diameter. However, this limitation was alleviated when a large number of boundary pixels were evaluated and presented statistically. Reasonably accurate estimations of diameters of capillary tube phantom and kidney tubules were achieved through this algorithm, as confirmed by digital microscopy and histology. To overcome these limitations completely, future development of 3D boundary and skeleton recognition algorithms would be an ultimate solution.

We should note as well that the present image analysis method cannot automatically separate different objects which are slightly connected to each other such as glomerulus and its associated tubules. In the image processing of human kidney microstructures obtained by optical OCT, one challenging step is to separate different microstructures which are slightly 'touching' each other. For instance, the glomerulus needs to be separated from its associated proximal tubule for image processing consideration, although they are physically connected to each other. Two approaches are proposed in the following paragraphs.

The first approach is based on image opening. Images to be separated are binary images since they are the image features extracted by image segmentation. Therefore, morphological operations are suitable to be applied on these images. Basic morphological operations include erosion and dilation. Erosion shrinks image objects while dilation expands them. Dilation and erosion are often applied to an image in concatenation. An erosion followed by a dilation is called image opening, which can separate objects

connected in a binary image. The specific actions of each operation are illustrated in the figure 23 [45].

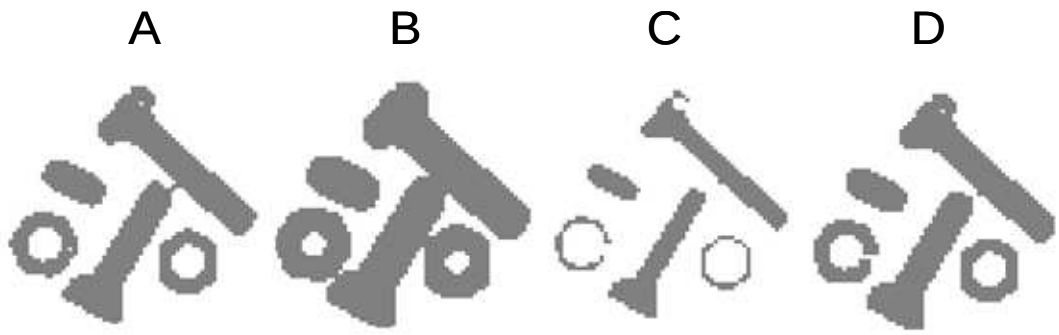

Fig. 23. Examples of various mathematical morphology operations: A) original image; B) dilation; C) erosion; D) image opening.

According to the result of image opening showed in fig. 23, image opening shows to be a feasible approach for separation of different connected microstructures. Image opening operation generates a certain amount of smoothing on an object contour and especially smoothes from the inside of the object contour. In order to disconnect different objects and at the same time preserve as much of the original images as possible, the structuring element used to do image erosion and dilation should be selected carefully. Too large of a structuring element will lead to image distortion, while too small of a structuring element can only break thin connections.

The second approach lies on watershed transformation. Figure 24 illustrates a glomerulus connected by a proximal tubule.

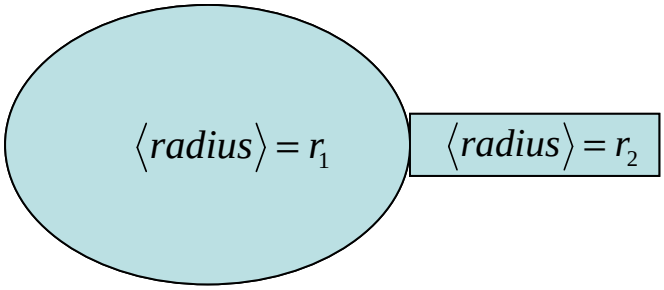

Fig. 24 Illustration of a glomerulus connected with a proximal tubule

First of all, the radii of all pixels on the boundary are calculated. Since the radius of the glomerulus (r1) is significantly greater than that of the tubule (r2), the histogram of radii distribution will have at least two peaks. By judging the radii histogram, all connected images with different microstructures are distinguished. Finally, watershed transformation can be used to separate the images characterized as an oval (glomerulus) connected by narrow tubes (tubules). This approach works for images with special morphologies as illustrated in the fig. 24. However, it is impossible to differentiate images showing ring shape connected with tubes because the radii of the ring are similar to that of the tubes.

Although the present OCT system has a limited resolution of 10 µm, it is still sufficient to detect the tubules in the human kidney. We observed tubular diameters range from 30 - 60 µm from four human kidneys after formalin fixation. From the literature, normal human proximal convoluted tubule has a diameter of approximately 55 µm [46]. The ultimate clinical utility of this method will be assessed by the clinical evaluation of kidney viability, where the threshold tubular diameter for viable kidney can be determined.

Finally, along with the complexity of the processing methods, time economics become another issue especially when a real-time processing is required. One way to speed up the implementation is to translate this algorithm into more efficient programming language, i.e. C++.

6.2 Conclusion

OCT is a rapidly developing imaging modality that can produce 3D imaging of tissue *in situ* and in real time. OCT can provide cross-sectional images which make 3D reconstruction and image processing possible. It can visualize tissue microstructure without the need for contact or tissue removal, thereby facilitating sterility and minimizing possible damage to the tissue. The high resolution capability of OCT is sufficient for imaging numerous organs such as the human kidney.

In this study, OCT imaging of human kidney was visualized in real time. Automated image analyses algorithms have been developed for quantifying spatially-resolved tubular diameter as a biomarker for kidney viability. Images along the three orthogonal image-planes (XY, YZ, and XZ) in the Euclidean space were displayed sequentially. Moreover, the rendering of the images provided a 3D volumetric view. The computed microstructure sizes were then color-coded on the reconstructed images, revealing quantitative information of the kidney microanatomy. Based on the results of this study, we have demonstrated the capability of OCT imaging and automated quantification of human kidney microanatomy. Automated image classification is also successfully implemented to separate three classes of human kidney microstructures: glomeruli, blood vessels, and tubules. The ability of OCT to provide 3D, high resolution imaging illustrates the potential of using OCT to image donor kidney structures and to

evaluate the organ's viability, or image the responses to acute kidney injuries. Automated image processing algorithm in the current study helps researchers to handle a large volume of data set in real time, which will promote OCT image technology from 'bench side' to 'bed side'.

6.3 Future Work

Future work will involve the quantification of more parameters like the curvature for human kidney images and compare them with the histopathology for diagnostic calibration.

In addition, those parameters should be quantified for different human kidneys to obtain the baseline values for diagnostic purposes, and perform OCT images for human kidney *in vivo* to examine the correlation between the dimensions of their imaged features and post-transplantation renal function, or further analyze and diagnose kidney diseases.

The image classification could be improved in other novel ways. Recently Miyazawa et al. [47] developed a tissue discrimination algorithm of polarization sensitive optical coherence tomography (PS-OCT) based on the optical properties of tissues. They calculated the three-dimensional (3D) feature vector from the parameters intensity, extinction coefficient, and birefringence and determined the tissue type of each pixel according to the position of the feature vector in the 3D feature space. The conjunctiva, sclera, trabecular meshwork (TM), cornea, and uvea were well separated in the 3D feature space as they reported.

Research is ongoing and future improvement should concentrate on developing more efficient and effective algorithms for OCT image processing. The algorithms must also increase in accuracy in order to be reliable for the everyday user.

REFERENCES

[1] D. Huang, E.A. Swanson, C.P. Lin, J.S. Schuman, W.G. Stinson, W. Chang, M.R. Hee, T. Flotte, K. Gregory, C.A. Puliafito, and J.G. Fujimoto, "Optical coherence tomography," Science, **254,** 1178-1181 (1991).

[2] K.W. Gossage, T.S. Tkaczyk, J.J. Rodriguez, and J.K. Barton, "Texture analysis of optical coherence tomography images: feasibility for tissue classification," Journal of biomedical optics, **8,** 570-5 (2003).

[3] X. Qi, M.V. Sivak, G. Isenberg, J.E. Willis, and A.M. Rollins, "Computer-aided diagnosis of dysplasia in Barrett's esophagus using endoscopic optical coherence tomography," Journal of biomedical optics, **11,** 044010 (2006).

[4] X. Qi, Y. Pan, Z. Hu, W. Kang, J.E. Willis, K. Olowe, M.V. Sivak, Jr., and A.M. Rollins, "Automated quantification of colonic crypt morphology using integrated microscopy and optical coherence tomography," Journal of biomedical optics, **13,** 054055 (2008).

[5] Y. Chen, A.D. Aguirre, P. Hsiung, S.W. Huang, H. Mashimo, J.M. Schmitt, and J.G. Fujimoto, "Effects of Axial Resolution Improvement on Optical Coherence Tomography (OCT) Imaging of Gastrointestinal Tissues," Optics express, **16,** 2469-2485 (2008).

[6] M.R. Hee, J.A. Izatt, E.A. Swanson, D. Huang, J.S. Schuman, C.P. Lin, C.A. Puliafito, and J.G. Fujimoto, "Optical coherence tomography of the human retina," Archives of Ophthalmology, **113,** 325-332 (1995).

[7] W. Drexler, H. Sattmann, B. Hermann, T.H. Ko, M. Stur, A. Unterhuber, C. Scholda, O. Findl, M. Wirtitsch, J.G. Fujimoto, and A.F. Fercher, "Enhanced visualization of macular pathology with the use of ultrahigh-resolution optical coherence tomography," Archives of Ophthalmology, **121,** 695-706 (2003).

[8] M. Wojtkowski, V. Srinivasan, J.G. Fujimoto, T. Ko, J.S. Schuman, A. Kowalczyk, and J.S. Duker, "Three-dimensional retinal imaging with high-speed ultrahigh-resolution optical coherence tomography," Ophthalmology, **112,** 1734-46 (2005).

[9] J.G. Fujimoto, S.A. Boppart, G.J. Tearney, B.E. Bouma, C. Pitris, and M.E. Brezinski, "High resolution in vivo intra-arterial imaging with optical coherence tomography," Heart, **82,** 128-33 (1999).

[10] I.K. Jang, B.E. Bouma, D.H. Kang, S.J. Park, S.W. Park, K.B. Seung, K.B. Choi, M. Shishkov, K. Schlendorf, E. Pomerantsev, S.L. Houser, H.T. Aretz, and G.J. Tearney, "Visualization of coronary atherosclerotic plaques in patients using optical coherence tomography: comparison with intravascular ultrasound," Journal of the American College of Cardiology, **39,** 604-9 (2002).

[11] B.E. Bouma, G.J. Tearney, C.C. Compton, and N.S. Nishioka, "High-resolution imaging of the human esophagus and stomach in vivo using optical coherence tomography," Gastrointestinal Endoscopy, **51,** 467-74 (2000).

[12] M.V. Sivak, Jr., K. Kobayashi, J.A. Izatt, A.M. Rollins, R. Ung-Runyawee, A. Chak, R.C. Wong, G.A. Isenberg, and J. Willis, "High-resolution endoscopic imaging of the GI tract using optical coherence tomography," Gastrointestinal Endoscopy, **51,** 474-9 (2000).

[13] X.D. Li, S.A. Boppart, J. Van Dam, H. Mashimo, M. Mutinga, W. Drexler, M. Klein, C. Pitris, M.L. Krinsky, M.E. Brezinski, and J.G. Fujimoto, "Optical

coherence tomography: advanced technology for the endoscopic imaging of Barrett's esophagus," Endoscopy, **32,** 921-30 (2000).
[14] Y. Chen, A.D. Aguirre, P.L. Hsiung, S. Desai, P.R. Herz, M. Pedrosa, Q. Huang, M. Figueiredo, S.W. Huang, A. Koski, J.M. Schmitt, J.G. Fujimoto, and H. Mashimo, "Ultrahigh resolution optical coherence tomography of Barrett's esophagus: preliminary descriptive clinical study correlating images with histology," Endoscopy, **39,** 599-605 (2007).
[15] J.G. Fujimoto, "Optical coherence tomography for ultrahigh resolution in vivo imaging," Nature Biotechnology, **21,** 1361-1367 (2003).
[16] *http://kidney.niddk.nih.gov/kudiseases/pubs/transplant/*.
[17] P.M. Andrews, B.S. Khirabadi, and B.C. Bengs, "Using tandem scanning confocal microscopy to predict the status of donor kidneys," Nephron, **91,** 148-55 (2002).
[18] S. Daiman and I. Koni, "Glomerular enlargement in the progression of mesangial proliferative glomerulonephritis," Clin. Nephrol., **49,** 145-152 (1998).
[19] E. Nyberg, S.O. Bohman, and U. Berg, "Glomerular volume and renal function in children with different types of nephrotic syndrome," Pediatr. Nephrol., **8,** 285-289 (1994).
[20] H.J. Gunderson and R. Osterby, "Glomerular size and structure in diabetes mellitus II. Late abnormalities," Disbetologia **13,** 43-48 (1977).
[21] K. Moran, J. Mulhall, D. Kelly, S. Sheehan, J. Dowsett, P. Dervan, and J.M. Fitzpatrick, "Morphological changes and alterations in regional intrarenal blood flow induced by graded renal ischemia," The Journal of urology, **148,** 463-6 (1992).
[22] Y. Chen, P.M. Andrews, A.D. Aguirre, J.M. Schmitt, and J.G. Fujimoto, "High-resolution three-dimensional optical coherence tomography imaging of kidney microanatomy ex vivo," Journal of biomedical optics, **12,** 034008 (2007).
[23] P.M. Andrews, Y. Chen, M.L. Onozato, S.W. Huang, D.C. Adler, R.A. Huber, J. Jiang, S.E. Barry, A.E. Cable, and J.G. Fujimoto, "High-resolution optical coherence tomography imaging of the living kidney," Laboratory investigation; a journal of technical methods and pathology, **88,** 441-9 (2008).
[24] O.B. Franc, C. Stefano, V.S. Maria, G. Lorenzo, H. Yale, T. Stefano, and S. Antonio, "Automatic evaluation of arterial diameter variation from vascular echographic images," Ultrasound in Med. & Biol., **27,** 1621-1629 (2001).
[25] V. Gemignani, F. Faita, L. Ghiadoni, E. Poggianti, and M. Demi, "A system for real-time measurement of the brachial artery diameter in B-mode ultrasound images," IEEE transactions on medical imaging, **26,** 393-404 (2007).
[26] R. Huber, M. Wojtkowski, and J.G. Fujimoto, "Fourier Domain Mode Locking (FDML): A new laser operating regime and applications for optical coherence tomography," Optics express, **14,** 3225-3237 (2006).
[27] M.A. Choma, M.V. Sarunic, C.H. Yang, and J.A. Izatt, "Sensitivity advantage of swept source and Fourier domain optical coherence tomography," Optics express, **11,** 2183-2189 (2003).
[28] J.M. Schmitt, S.H. Xiang, and K.M. Yung, "Speckle in optical coherence tomography," Journal of biomedical optics, **4,** 95-105 (1999).
[29] J. Rogowska and M.E. Brezinski, "Image processing techniques for noise removal, enhancement and segmentation of cartilage OCT images," Physics in Medicine and Biology, **47,** 641-55 (2002).

[30] M.E. Brezinski, *Optical Coherence Tomography: Principles and Applications*. 2006: Elsevier Inc.
[31] D. Lei *Quantitative analysis of tumor microvascular density*. **Volume**, 1-38
[32] A. Yazdanpanah, *Intra-retinal Layer Segmentation in Optical Coherence Tomography Using an Active Contour Approach*, in *MICCAI 2009*. 2009, Springer-Verlag: London, UK. p. 649-656.
[33] D. Cabrera Fernandez, H.M. Salinas, and C.A. Puliafito, "Automated detection of retinal layer structures on optical coherence tomography images," Optics express, **13,** 10200-16 (2005).
[34] G. Gilboa, N. Sochen, and Y.Y. Zeevi, "Image enhancement and denoising by complex diffusion processes," IEEE transactions on pattern analysis and machine intelligence, **26,** 1020-36 (2004).
[35] J. Weickert, "Coherence-enhancing diffusion filtering," Int. J. Comput. Vision, **31,** 111-127 (1999).
[36] R.C. Gonzalez and R.E. Woods, *Digital mage Processing*. Third Edition ed. 2008.
[37] L. Lam, S.-W. Lee, and C.Y. Suen, "Thinning Methodologies-A Comprehensive Survey," IEEE Transactions on Pattern Analysis and Machine Intelligence, **14,** 879 (1992).
[38] T.J. Hall, M.F. Insana, L.A. Harrison, and G.G. Cox, "Ultrasonic measurement of glomerular diameters in normal adult humans," Ultrasound Med Biol, **22,** 987-97 (1996).
[39] M. Sonka, V. Hlavac, and R. Boyle, *Image Processing, Analysis, and Machine Vision*. Third ed. 2008: Thomson Learning.
[40] R.S. Sabeenian and V. Palanisamy, "Texture-based medical image classification of computed tomography images using MRCSF," International Journal of Medical Engineering and Informatics **1,** 459 - 472 (2009).
[41] N.A. Nassif, B. Cense, B.H. Park, M.C. Pierce, S.H. Yun, B.E. Bouma, G.J. Tearney, T.C. Chen, and J.F. de Boer, "In vivo high-resolution video-rate spectral-domain optical coherence tomography of the human retina and optic nerve," Optics express, **12,** 367-376 (2004).
[42] R.A. Leitgeb, W. Drexler, A. Unterhuber, B. Hermann, T. Bajraszewski, T. Le, A. Stingl, and A.F. Fercher, "Ultrahigh resolution Fourier domain optical coherence tomography," Optics express, **12,** 2156-2165 (2004).
[43] M. Wojtkowski, V.J. Srinivasan, T.H. Ko, J.G. Fujimoto, A. Kowalevicz, and J.S. Duker, "Ultrahigh resolution, high speed, Fourier domain optical coherence tomography and methods for dispersion compensation," Optics express, **12,** 2404-2422 (2004).
[44] R. Huber, M. Wojtkowski, J.G. Fujimoto, J.Y. Jiang, and A.E. Cable, "Three-dimensional and C-mode OCT imaging with a compact, frequency swept laser source at 1300 nm," Optics express, **13,** 10523-10538 (2005).
[45] *http://www.ph.tn.tudelft.nl/Courses/FIP/noframes/fip-Segmenta.html#Heading121*.
[46] W.F. Ganong, *Review of Medical Physiology*. 2005: The McGraw-Hill Companies.
[47] A. Miyazawa and M. Yamanari, "Tissue discrimination in anterior eye using three optical parameters obtained by polarization sensitive optical coherence tomography," Optics express, **17,** 17426-17440 (2009).